Noble Gas Collision Induced Vibrational Relaxation of $(v = 1)$ *para*-H_2

by

Douglas B. Weir

A thesis
presented to the University of Waterloo
in fulfilment of the
thesis requirement for the degree of
Master of Science
in
Chemistry

Waterloo, Ontario, Canada, 2001

I hereby declare that I am the sole author of this thesis.

This is a true copy of the thesis, including any required final revisions, as accepted by my examiners.

I understand that my thesis may be made electronically available to the public.

Abstract

Close coupling scattering calculations have been conducted for the *para* spin modification of H_2-{He, Ne and Ar}. The `XC(fit)` potential energy surfaces for H_2-Ne and H_2-Ar have been used for calculations for these two systems, while a newly fitted version of the Schaefer and Köhler potential energy surface was used for the H_2-He system. The fitting procedure employs nine modified Lennard-Jones oscilator functions to describe accurately 90% of the original tabulated potential energy surface to better than 12% error. The scattering calculations for H_2-Ar failed at higher energies due to the presence of a previously undocumented potential energy surface turn-over at $R < 1.0$ Å. Manifold-to-manifold $v = 1$ vibrational relaxation calculations for each of these systems are compared with other experimental and theoretical calculations. These comparisons demonstrate a common discrepancy between previous calculations and the current calculations for each system. The current vibrational relaxation rate constants are generally too small when compared to low temperature values of Audibert *et al.* and Orlikowski, and the high temperature values obtained by Flower *et al.* and Dove and Teitelbaum. The current calculations indicate the presence of a dramatic up-turn in the low temperature H_2-He rate constants. Other experimental and theoretical treatments do not exhibit this same up-turn, which is puzzling. A set of follow-up calculations featuring a larger basis set (such as the {16,12,10,8} Flower *et al.* basis set) and a larger manifold of included relaxation pathways are needed to improve these calculations.

Acknowledgements

The chain of events that have lead me up to this point are, to say the least, fascinating. There are several people who have been instrumental in shaping this chain of events, and I would like to express my gratitude for their part in this work (in chronological order);

My parents - their part in this work can not be overstated. This work is a testament to the 26 years worth of effort they have invested in me. From personally intervening when I was floundering in grade nine math, to piquing my interest in all things scientific at an early age.

My sister - she may not realise it, but her little brother had big shoes to fill growing up in her shadow. If she hadn't set the standard of excellence so high, I doubt that I would have had the motivation to work as hard as I did.

Ryan Port and **Duncan McIntyre** - these guys were in the trenches with me during high school and university, respectively. They are like brothers to me and I am in debt to them both.

Dr. Bob Le Roy - the frequent discussions about least square fitting, quantum mechanics and his suite of computer programs were an invaluable part of this research. The opportunity to manage the various UNIX research computers is greatly appreciated as well.

Dr. Wing-Ki Liu - our weekly scattering theory discussions greatly improved my understanding of this complicated field. The opportunity to co-author part of a chapter of a physics handbook with him is also a great honour.

Dr. Fred McCourt - it is impossible to say how different things would have been if he had not convinced me (at the last minute) to stay at Waterloo work with him on this graduate degree. I am deeply grateful for his patience and guidance during this work, as well as his commitment to quality teaching which I was lucky enough to witness three times.

Me - let's face it, I did most of the work here, so I should at least get an acknowledgment. :)

"An expert is a man who has made all the mistakes which can be made, in a very narrow field."

Niels Bohr (1885–1962)

Contents

1 Introduction **1**

1.1 *What is it?* . . . 2

1.2 *Why is it relevant ?* . . . 2

1.3 *What is gained by studying it?* . . . 3

2 Theory **5**

2.1 Atom-Diatom Inelastic Scattering Theory . . . 6

2.2 Kinetic Theory . . . 10

3 Calculations **15**

3.1 Potential Energy Surfaces . . . 16

3.2 The `XC(fit)` Potentials: H_2-Ar and H_2-Ne . . . 18

3.3 The H_2-He Potential . . . 21

3.3.1 The Diatom Bond Length Coordinate, r . . . 22

3.3.2 The MLJ and the Atom-Diatom Separation Coordinate, R . . . 25

3.4 `MOLSCAT` . . . 41

3.4.1 The Scattering Basis Set . . . 42

3.4.2 Integration Parameters . . . 47

3.5 Thermal Averaging and Rate Constants . . . 54

4 Results and Discussion **58**

4.1 Previous Experimental Results 59

4.2 Previous Theoretical Results 62

4.3 The Current Results 66

5 Summary **75**

A H_2-He Parameters **77**

Bibliography **79**

List of Tables

3.1 The "rule of thumb" basis set. 43

4.1 Additional vibrational relaxation pathways incorporated by Flower *et al.* 65

4.2 The energy integration ranges used for the various versions of the current data. . . 66

A.1 MLJ (12,6) parameters for the $W_{0k}(R)$ and $W_{2k}(R)$ components of H_2-He. 77

A.2 Exponential parameters for the $W_{4k}(R)$ components of H_2-He. 78

List of Figures

2.1 The center-of-mass frame of reference. 7

2.2 Fractional populations of various sized initial state manifolds. 13

3.1 An illustration of the pathological short-range potential turn-over for H_2-Ar 20

3.2 The $W_{0k}(R)$ potential components. 34

3.3 The $W_{2k}(R)$ potential components. 35

3.4 The $W_{4k}(R)$ potential components. 36

3.5 The absolute differences of the fitted versus tabulated H_2-He potential. 38

3.6 A histogram of percent errors of the fitted versus tabulated H_2-He potential. . . . 40

3.7 The basis set convergence tests at $E = 5000$ cm^{-1}. 45

3.8 The basis set convergence tests at $E = 6000$ cm^{-1}. 46

3.9 The scattering calculation time as a function of basis set size and system. 48

3.10 The `RMAX` convergence tests at E = 5000 cm^{-1} 51

3.11 The `RMAX` convergence tests at E = 6000 cm^{-1} 52

3.12 A test calculation of H_2-He using two different propagators. 53

3.13 An illustration of the manifold of cross sections calculated for H_2-Ne 55

3.14 The energy dependence of the H_2-He rate constant integrand. 57

4.1 ($v = 1$) Manifold-to-manifold vibrational relaxation rate constants for H_2-He. . . . 69

4.2 ($v = 1$) Manifold-to-manifold vibrational relaxation rate constants for H_2-Ne. . . . 71

4.3 ($v = 1$) Manifold-to-manifold vibrational relaxation rate constants for H_2-Ar. . . . 72

Chapter 1

Introduction

Vibrational relaxation. *What is it ? Why is it relevant ? What is gained by studying it ?* Before investing vast amounts of time, effort and money into studying a particular field, such as vibrational relaxation, these three questions must be answered. At first glance these question seem to be nothing more than simple queries about the problem. However, upon closer inspection the larger meaning which they embody becomes clear. By answering the first question - *What is it?* - the nebulous concept of problem takes a solid well-defined form. Attempting to solve problems which lack definition is a duty best left to psychics and clairvoyants. The second question - *Why is it relevant ?* - places the clearly-defined problem into a familiar context. A problem which lacks a context can lead to academic pursuits and intellectual "wheel-spinning", neither of which contribute to the general or scientific community at large. The third and final question - *What is gained by studying it ?* - provides the motivation needed to propel the research forward. Without an incentive, the original purpose of the research fades and the research stalls. In the following sections, each of these questions will be addressed in terms of the current problem - noble gas collision induced vibrational relaxation of $(v = 1)$ *para*-H_2.

1.1 *What is it?*

In the most general terms, vibrational relaxation can be defined as any mechanism which permits a rotationally-vibrationally (henceforth condensed to "rovibrationally") excited molecule to undergo a non-radiative transition to another less-energetic, less-vibrationally excited rovibrational state. In terms of the work presented here, this definition will be limited to the atom-diatom inelastic collision mechanism, with particular attention to noble gas atoms colliding with singly-vibrationally excited states of the *para* spin modification of H_2. Such systems represent the simplest systems which can undergo vibrational relaxation processes. These simplifications come from several places; the isotropic electron charge distribution surrounding the noble gas atom, the low reduced mass of H_2, and the *ortho-*/*para-* spin modification separability found in all homonuclear diatomic molecules, to name a few. The isotropic electron charge distribution of the noble gas atom simply means that there is no intrinsic angular momentum carried by the noble gas atom which would need to be taken into consideration during the scattering calculations. Low reduced mass diatomic molecules possess larger rotational level spacings, which helps to reduce the number of energetically accessible basis states that would need to be included in the scattering calculations. The *ortho-*/*para-* spin modifications of H_2 also serve to reduce the number of accessible basis states by separating the even and odd numbered rotational levels into two totally independent species.

1.2 *Why is it relevant ?*

Studying noble gas collision-induced vibrational relaxation of *para*-H_2 may seem somewhat academic, but the truth of the matter is that this topic has several important applications. Hydrogen is the most abundant element, corresponding to approximately 90% of all visible matter in the universe [1]. The next most abundant element is helium, a distant second representing only about 9% of the visible matter in the universe. Most of the hydrogen in the universe is found in dense interstellar clouds in the energetically more-favourable diatomic molecular form, while helium is

exclusively found in its atomic form. With diatomic hydrogen and atomic helium comprising the bulk of the visible universe, studying H_2-He and other H_2-Ng (Ng = noble gas) systems in general has many diverse applications in the fields of astronomy, astrophysics, and cosmology.

1.3 *What is gained by studying it?*

The short answer to this question is simple, added knowledge about molecular hydrogen is gained by studying its collision-induced vibrational relaxation. This in itself is reason enough to study it; however, the longer answers to this question are much more satisfying. Since molecular hydrogen is the most common molecule in the entire universe the application of this added knowledge are potentially limitless. The vibrational relaxation rate constant data can be used to improve models of: the early hydrogen/helium rich universe, the dense molecular clouds in the present-day universe, stars, and the atmospheres of gas giants, to name just a few astrophysical/cosmological applications.

On a less grandiose scale, vibrational relaxation calculations can also serve as a valuable diagnostic tool to researchers attempting to generate accurate potential energy surfaces. In the case of H_2-Ar, Bissonnette *et al.* have spent a great deal of effort generating a spectroscopically accurate `XC(fit)` potential energy surface [2]. While their test calculations using this potential energy surface demonstrate good agreement with experimentally measured infrared spectral data, second virial coefficients and Raman line-shifting coefficients, Waldron [3] has discovered a significant discrepancy between the polarised $Q_1(1)$ line-width coefficients calculated using their potential and the experimental measurements of Berger *et al.* [4]. The $Q_1(1)$ Raman spectral line represents a rotationally elastic, vibrationally inelastic diatomic transition from $(v = 1, j = 1) \rightarrow (v = 0, j = 1)$ whose prediction depends on the accuracy of the diatom stretching dependence of the potential energy surface. The discrepancy noted by Waldron suggests that the stretching dependence of the `XC(fit)` H_2-Ar potential energy surface may be inadequate. Vibrational relaxation calculations

are also very sensitive to the diatom stretching dependence of the potential energy surface, and can serve as another reliable independent method of assessing the quality of the H_2-Ar surface.

Chapter 2

Theory

The complete theory describing vibrational relaxation of diatomic molecules can be expounded to fill several hundred pages. In some circles, such an attention to detail is crucial to the understanding of the problems at hand. More often than not however, the subtleties documented in such careful derivations can often serve to obfuscate the nature of the problem at hand, rather than clarify it. In this chapter, a great deal of care has been employed to ensure that the discussion incorporates a sufficient level of detail so that a true representation of the problem at hand is documented, while attempting to avoid the quagmire of unnecessary details.

Like most quantum mechanical discussions, it begins with the notion of a wavefunction. The wavefunction, in perhaps the broadest definition, is simply a complete representation of a system. All of the accessible information about the system is carried by the wavefunction, and any part of this information can be extracted through the judicious use of the appropriate operator. An operator is a mathematical device which performs a specific mathematical operation on another object. This operation can be as simple as multiplying the target object by some factor, as is the case for the x-position operator $\hat{x} = x$, or it can involve much higher level mathematics resulting in a comparatively more complicated operator such as the magnitude of the angular momentum

operator,

$$\hat{L}^2 = \frac{1}{\sin\theta}\frac{\partial}{\partial\theta}\left(\sin\theta\frac{\partial}{\partial\theta}\right) + \frac{1}{\sin^2\theta}\frac{\partial^2}{\partial\phi^2}. \tag{2.1}$$

The *Third Postulate of Quantum Mechanics* states that for every physical observable there exists an operator which can extract information pertaining to this observable from the wavefunction describing the system [5]. One such operator is the Hamiltonian $\hat{H}$, which is used to extract the total energy E_n from the wavefunction Ψ_n describing a system in a particular state of the system designated by the label n:

$$\hat{H}\Psi_n = E_n\Psi_n \tag{2.2}$$

This is the time-independent Schrödinger equation, one of the most important equations of the 20th century. It is this equation that underpins innumerable quantum mechanical discussions, and it is the best place to begin a discussion of quantum mechanical atom-diatom inelastic scattering.

2.1 Atom-Diatom Inelastic Scattering Theory

In the centre-of-mass frame of reference, let there be a structureless atom separated from the centre-of-mass of a diatomic molecule by a position vector $\mathbf{R}$. Similarly, let $\mathbf{r}$ represent the position vector which defines the bond length and orientation of the diatomic molecule with respect to the position of the atom. The relative orientation angle θ created by these two vectors is defined as $\theta = \arccos(\mathbf{e_R} \cdot \mathbf{e_r})$, where $\mathbf{e_R}$ and $\mathbf{e_r}$ are unit vectors pointing along the directions of $\mathbf{R}$ and $\mathbf{r}$ respectively. The Hamiltonian for the atom-diatom system in this frame of reference is given by

$$\hat{H} = -\frac{\hbar^2}{2m}\nabla_r^2 - \frac{\hbar^2}{2\mu}\nabla_R^2 + v(r) + V(R, r, \theta). \tag{2.3}$$

Where m is the reduced mass of the diatomic molecule and μ is the reduced mass of the atom with respect to the diatomic molecule. The first term represents the internal kinetic energy of the diatomic molecule (such as rotational and vibrational kinetic energy), the second term represents the relative translational kinetic energy of the collision pair, the third term is the internal potential energy function of the isolated diatomic molecule, and the fourth term is the

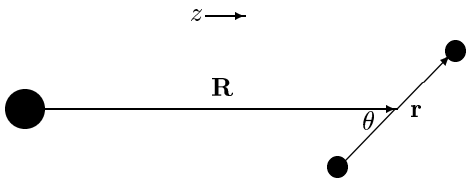

Figure 2.1: Centre-of-mass frame of reference displaying the Jacobi coordinates and the direction of the space-fixed z-axis.

atom-diatom interaction potential energy surface. Quantum states of the atom-diatom system are labeled by the values of the diatomic vibrational quantum number v, the diatomic rotational angular momentum quantum number j, and by the atom-diatom orbital angular momentum quantum number l. It should be noted that due to the identical particle symmetry of H_2 there exist two independent spin modifications: one in which the rotational angular momentum quantum number j is restricted to even values only (referred to as *para*-H_2), and another in which j is restricted to odd values only (referred to as *ortho*-H_2). The research contained herein is exclusively interested in the even rotational angular momentum levels of the *para*-H_2 spin modification. In addition to the vjl quantum number labels, it is a common practise to also include the total angular momentum $|j-l| \leq J \leq j+l$ and its projection $M = m_j + m_l$ on the space-fixed z-axis, since the total angular momentum is a constant of motion. This means that a wavefunction describing a state of the system can be written as $\Psi_{vjl}^{JM}(R,r,\theta)$. The time-independent Schrödinger equation (2.2) can now be rewritten as

$$\left(-\frac{\hbar^2}{2m}\nabla_r^2 - \frac{\hbar^2}{2\mu}\nabla_R^2 + v(r) + V(R,r,\theta)\right)\Psi_{vjl}^{JM}(R,r,\theta) = E_{vj}\Psi_{vjl}^{JM}(R,r,\theta). \tag{2.4}$$

A common approach to solving this equation is to expand the total wavefunction as the summed products of extramolecular and intramolecular pieces,

$$\Psi_{vjl}^{JM}(R,r,\theta) = \frac{1}{rR}\sum_{v'j'l'}^{\infty} u_{v'j'l'}^{Jvjl}(R)\phi_{v'j'l'}^{JM}(r,\theta), \tag{2.5}$$

where $u^{Jvjl}_{v'j'l'}(R)$ and $\phi^{JM}_{v'j'l'}(r,\theta)$ represent the extramolecular and intramolecular parts of the total wavefunction, respectively. By substituting this expanded version of the total wavefunction (2.5) into the time-independent Schrödinger equation (2.4) a considerable simplification can be made, ultimately resulting [6, 7] in

$$\left[\frac{d^2}{dR^2} - \frac{l(l+1)}{R^2} + \frac{2\mu}{\hbar^2}\epsilon_{vj}\right] u^{Jvjl}_{vjl}(R) = \sum_{v'j'l'}^{\infty} u^{Jvjl}_{v'j'l'}(R)\langle vjl; J|V(R,r,\theta)|v'j'l'; J\rangle, \tag{2.6}$$

where,

$$\langle vjl; J|V(R,r,\theta)|v'j'l'; J\rangle \equiv 2\pi \int_0^{\pi}\int_0^{\infty} \phi^{JM}_{vjl}(r,\theta)V(R,r,\theta)\phi^{JM}_{v'j'l'}(r,\theta)r^2\sin^2\theta\; drd\theta, \tag{2.7}$$

and ϵ_{vj} represents the kinetic energy associated with the vjth state. Unfortunately, this equation is impossible to solve due to the infinite summation over the quantum states of the system. Within an acceptable level of inaccuracy (imposed by the user) however, this summation can be truncated to include only those quantum states that are strongly coupled. The finite set of coupled differential equations resulting from this truncation of the summation in (2.6) is referred to as the *close-coupling equations*. Solving the close-coupling equations is a pivotal step in creating the wavefunctions $\Psi^{JM}_{vjl}(R,r,\theta)$ that describe the system after a scattering event has occurred.

Experimentally, a scattering event occurs over a very small length scale as compared to the distance the scattered particles must travel before arriving at some form of detector. Theoretically, this notion of interrogating the products of the scattering process after they have traveled a large distance from the scattering region can be reproduced by examining the post-collision wavefunction at asymptotically large values of the atom-diatom separation, R. The extramolecular wavefunction $u^{Jvjl}_{v'j'l'}(R)$, which is the only part of the total wavefunction $\Psi^{JM}_{vjl}(R,r,\theta)$ that depends upon the atom-diatom separation R, will have two terms in its asymptotic form. One term representing the incoming flux of particles in the state vjl, and a second term representing

an outgoing flux of scattered particles in the state $v'j'l'$ [8, 9],

$$u^{Jvjl}_{v'j'l'}(R \to \infty) = \delta_{vv'}\delta_{jj'}\delta_{ll'}e^{-i(k_{vj}R - l\pi/2)} - \frac{k_{vj}}{k_{v'j'}}\mathsf{S}^{J}_{vjl\to v'j'l'}(E)e^{i(k_{v'j'}R - l\pi/2)} \tag{2.8}$$

Where $\delta_{vv'}$, $\delta_{jj'}$, and $\delta_{ll'}$ represent Kronecker delta functions, while $k^2_{vj} = 2\mu/\hbar^2(E - \epsilon_{vj})$, and the $\mathsf{S}^{J}_{vjl\to v'j'l'}(E)$ are the scattering or S-matrix elements. Armed with the asymptotic form of the extramolecular wavefunction $u^{Jvjl}_{v'j'l'}(R)$, there is now sufficient information to generate a quantity called the state-to-state total integral cross section. These cross sections provide an energy dependent description of the probability of a system in the initial diatomic "state" (v, j) being inelastically scattered into the final diatomic "state" (v', j'). The rather unwieldy name given to these cross sections is unfortunately necessary so as to identify clearly these specific cross sections from the plethora of other types of cross sections. The term *integral cross section* is used to signify that an integral over all scattering angles has been used to accumulate numerically all of the scattering products, irrespective of the direction in which they were scattered. The term *total integral cross section* signifies that a summation over all of the partial wave contributions (analogous to classical "impact parameters") has also been incorporated. Finally, the term *state-to-state total integral cross section* is a further delineation signifying that these cross sections only represent the scattering from one particular diatomic "state" (v, j) to another diatomic "state" (v', j') (integrated over all scattering angles, and summed over all partial waves). It should be stated that in the strictest parlance, these cross sections would actually be referred to as *level-to-level* total integral cross sections since there is no m_j projection quantum number discrimination. The absence of an external electric or magnetic field (which would lift some or all of the m_j degeneracy) serves to blur the distinction between level-to-level and state-to-state total integral cross sections. In an effort to conform with the majority of other works in this field, the less accurate term "state-to-state" will be adopted henceforth. Construction of these state-to-state total integral cross section begins by forming the ratio of the asymptotic scattered probability flux to the asymptotic incident probability flux. The actual mathematics involved in this derivation is far beyond the scope of this research and would most likely only serve to confuse the author and reader alike. A complete treatment of this and other related derivations can be found in work

by people such as Lester [8] and Arthurs and Dalgarno [6]. The state-to-state total integral cross section is hence defined as,

$$\sigma_{vj\to v'j'}(E) = \frac{\pi}{k_{vj}^2(2j+1)} \sum_{J=0}^{\infty}(2J+1) \sum_{l=|J-j|}^{J+j} \sum_{l'=|J-j'|}^{J+j'} |\delta_{vv'}\delta_{jj'}\delta_{ll'} - \mathsf{S}^J_{vjl\to v'j'l'}(E)|^2. \qquad (2.9)$$

These state-to-state total integral cross sections are the final product of a theoretical treatment of an atom-diatom scattering process. However, for the current purpose at hand they are merely one step in a sequence of calculations ultimately resulting in a rate constant for the collision induced vibrational relaxation of the diatomic molecule.

2.2 Kinetic Theory

As demonstrated above, scattering theory can successfully describe, for a given energy, the probability that the initial state of a diatom (v, j) is scattered into a final state (v', j') by way of an inelastic collision with an atomic projectile. The problem hitherto unaddressed is how a state-to-state total integral cross section will become an experimentally measurable rate constant.

From simple second-order kinetics, the rate of depletion of the population of diatoms in the initial state N_i is given by,

$$\frac{d}{dt}[N_i] = -k(\nu)[N_i][M], \qquad (2.10)$$

where $k(\nu)$ is the relative speed dependent collision rate constant, and M is the population of atomic projectiles. All else being equal, the more numerous the population of systems in the initial state, or the larger the collision rate constant, the greater the rate at which the population of systems in the initial state is depleted. By increasing the number of systems in the initial state there are essentially more targets to collide with, which results in an increased collision rate and hence an increased rate of depletion. When the collision rate constant $k(\nu)$ is increased however, the number of targets remain unchanged, but the number of collisions as well as the rate of depletion increases. Intuitively, the collision rate constant must incorporate some form of

collision probability factor to control, for a given relative speed ν, how likely it is that a collision will occur. This notion of a collision probability is intimately related to the previous discussions of scattering cross sections. The collision rate constant can be defined as the product of a scattering cross section $\sigma(\nu)$ and the relative speed of the colliding pair ν [10],

$$k(\nu) = \sigma(\nu)\ \nu. \tag{2.11}$$

By incorporating the state-to-state integral cross sections $\sigma_{vj\to v'j'}(\nu)$, a state-to-state collision rate constant can be generated,

$$k_{vj\to v'j'}(\nu) = \sigma_{vj\to v'j'}(\nu)\ \nu. \tag{2.12}$$

Experimental collision rate constants are measured at constant temperature rather than at a constant collision speed since it is physically impossible to generate a beam of particles having exactly the same speed. To incorporate this experimental limitation the relative-speed dependent state-to-state collision rate constants $k_{vj\to v'j'}(\nu)$, must be thermally averaged. To accomplish this thermal averaging, the distribution of systems having a relative speed between ν and $\nu + d\nu$ for a given temperature T, must be determined. The well-known Maxwellian speed distribution function $f(\nu)d\nu$ describes such a distribution of systems [11],

$$f(\nu)d\nu = \left(\frac{\mu}{2\pi k_B T}\right)^{3/2} \exp\left(-\frac{\mu\nu^2}{2k_B T}\right) 4\pi\nu^2 d\nu. \tag{2.13}$$

The thermally averaged state-to-state collision rate constant can now be defined as,

$$\langle k_{vj\to v'j'}(T)\rangle = \int_0^\infty k_{vj\to v'j'}(\nu) f(\nu) d\nu \tag{2.14}$$

$$= 4\pi \left(\frac{\mu}{2\pi k_B T}\right)^{3/2} \int_0^\infty \sigma_{vj\to v'j'}(\nu) \exp\left(-\frac{\mu\nu^2}{2k_B T}\right) \nu^3 d\nu. \tag{2.15}$$

While integration over the relative collision speed of the system is acceptable, it is more convenient for the task at hand to conduct this integration over the relative motion kinetic energy $E_k = \mu\nu^2/2$,

and hence the state-to-state collision rate constant can be rewritten as,

$$\langle k_{vj\to v'j'}(T)\rangle = \sqrt{\frac{8}{\pi\mu(k_BT)^3}}\int_0^\infty \sigma_{vj\to v'j'}(E_k)E_k\exp\left(-\frac{E_k}{k_BT}\right)dE_k. \tag{2.16}$$

The focus of this research is on vibrational relaxation rate constants; in particular, the $v = 1 \to v = 0$ vibrational relaxation rate constants. For a collision rate constant to be classified as a vibrational relaxation rate constant, there are two criteria that must be met. First, the vibrational quantum number of the initial state must be greater than that of the final state ($v > v'$) and second, the internal energy of the final state of the diatom must be less than the internal energy of the initial state. The final rotational level in $v = 0$ is not of particular interest in this work, so a summation over j' has been incorporated to accumulate numerically all of the available vibrational relaxation pathways from a given initial state in $v = 1$ to the manifold of all possible final vibrationally relaxed states in $v = 0$. As the temperature increases, higher initial rotational states will become thermally populated, and must be included in the manifold of initial states for completeness.

Figure 2.2 illustrates the fractional population of five different manifolds of initial states, varying from a single state , to a five-state manifold. To incorporate the effect of a manifold of initial states, a weighted sum over the states in the manifold is required. Simply put, each rotational state in the manifold of initial states, will possess a certain fraction of the total initial population. When incorporated into this sum over the manifold of initial states, this fractional population factor $\mathcal{P}_j(T)$ will weight each state-to-state vibrational relaxation rate constant based upon its thermal initial-state fractional population. The resulting expression for the thermally averaged, manifold-to-manifold vibrational relaxation rate constant is then expressed as

$$\langle k_{v=1\to v'=0}(T)\rangle = \sum_j \mathcal{P}_j(T)\int_0^\infty \sum_{j'} k_{1j\to 0j'}(\nu)f(\nu)d\nu, \tag{2.17}$$

where the fractional population factor $\mathcal{P}_j(T)$ is given by

$$\mathcal{P}_j(T) = \frac{(2j+1)\exp(-E_{v=1,j}/k_BT)}{\sum_{j''}(2j''+1)\exp(-E_{v=1,j''}/k_BT)}. \tag{2.18}$$

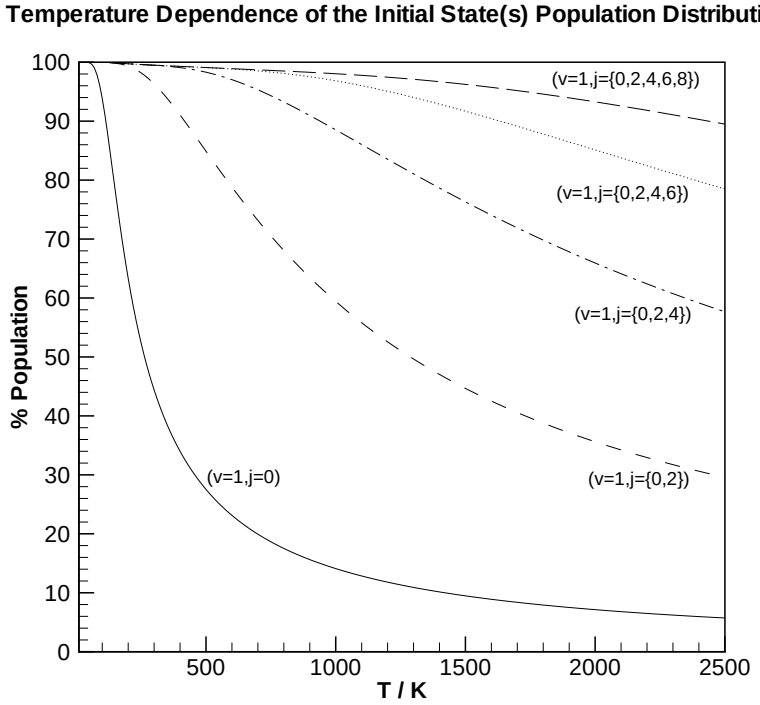

Figure 2.2: The percentage of the total population due to various initial state manifolds. Notice that as the temperature increases more and more rotational states are required to account for the bulk of the total population.

At lower temperatures ($T < 75$ K), the thermal population distribution of the initial states is almost entirely ($> 99\%$) represented by the single state ($v = 1, j = 0$), in which case the thermally averaged state-to-manifold vibrational relaxation rate constant is given by

$$\langle k_{v=1,j=0\rightarrow v'=0}(T)\rangle = \int_0^\infty \sum_{j'} k_{1j\rightarrow 0j'}(\nu) f(\nu) d\nu. \tag{2.19}$$

The state-to-manifold (Equation 2.19) and manifold-to-manifold (Equation 2.17) vibrational relaxation rate constants are quantities which are experimentally measurable. It should be noted that some vibrational relaxation experiments occur at high temperatures, resulting in thermal initial-state population distributions which not only span several rotational states in $v = 1$, but

also several rotational levels in $v = 2$ and beyond. Experimental data collected at temperatures in excess of ~ 2000K will be significantly influenced by these highly vibrationally excited ($v \geq 2$) species. The treatment heretofore discussed does not incorporate an initial state population distribution beyond $v = 1, j = 6$ and hence is not expected to describe reliably the results of any such high temperature experiments.

Chapter 3

Calculations

With the theoretical discussion of vibrational relaxation now complete, all that is left is to solve numerically the problems that these discussions have defined. Easier said than done. The elegance of a theoretical description and the ease of generating numerical solutions are not necessarily related. As shown in §2.1, the asymptotic form of the extramolecular wavefunction is relatively simple and straightforward, involving things like the fluxes of incoming and outgoing particles and S-matrix elements. The theoretical description of the asymptotic wavefunction is simple and compact. However, from a numerical processing standpoint, generating the S-matrix elements can be an exceedingly difficult task to accomplish. This chapter is dedicated to describing in detail the manner in which the theoretically-defined quantities from the previous chapter are turned into tangible numerical results. The roadmap of the calculations described herein is very similar to that of the previous theoretical discussion; scattering theory is employed to generate the state-to-state total integral cross sections, and then kinetic theory transforms these cross sections into the state-to-manifold/manifold-to-manifold vibrational relaxation rate constants. While the theoretical description of this process split the scattering theory and kinetic theory discussions into nearly equal sized sections, it will be shown that the actual numerical processing requirements of these two sections are far from equal.

There are two numerical packages [12, 13] available to the scientific community which can be used to solve the close-coupling equations and generate the state-to-state total integral cross sections that have been mentioned earlier. The calculations presented herein have been carried out using the general molecular inelastic scattering code of Hutson and Green called `MOLSCAT` [12]. The main reasoning behind this selection is that this package has been demonstrated to be a reliable method of solving similar problems in the past. It is very configurable, offering a great deal of control of the different automatic convergence criteria, a wide selection of different wavefunction propagators, and has the ability to employ any of several different approximation methods should the close-coupling treatment turn out to be more challenging than anticipated. `MOLSCAT` can be custom-built for each system by incorporating into the rest of the program a subroutine that describes the potential energy surface for that system. Before embarking on a discussion of the `MOLSCAT` calculations, the potential energy surfaces hitherto unexplained should be described.

3.1 Potential Energy Surfaces

In order to scatter one object off of another there must be a method of communicating some type of force between the objects, otherwise they would just pass one another as if the other wasn't even there. It may seem like a trivial point to mention, but it is the fundamental upon which all of scattering theory is based. The force $\mathbf{F}$ can be related to the gradient of a scalar field $U(\mathbf{r})$,

$$\mathbf{F} = -\nabla U(\mathbf{r}), \tag{3.1}$$

which simply states that the direction and magnitude of the force on an object located by $\mathbf{r}$ is determined by the direction and steepness of the steepest "slope" of $U(\mathbf{r})$. This scalar field is commonly referred to as a scalar potential. The concept of *potential energy* is a direct result of these scalar potentials. Instead of working in terms of forces which are vector quantities, quantum mechanical discussions tend to work in terms of potential energies (scalar potentials) because of

the simpler mathematics they require. Depending on the specific problem at hand, the potential energy may be a function of one variable, such as the separation of two objects, or it may be a function of several variables. When the potential energy depends on more than one variables, as is the case with the research contained herein, the potential energy is referred to as a potential energy surface (PES).

As alluded to earlier, it is the force communicated between two particles, and hence the potential energy surface that ultimately will cause the scattering of the two particles. Without an accurate description of the potential energy surface for the interaction, there can be no hope of modeling the scattering event. Potential energy surfaces can be constructed using many different techniques. Some are determined from the deconvolution of experimental data [14, 15], some are created from *ab initio* techniques [16, 17], and some potential energy surfaces are created using a combination of these techniques [18, 2]. The atomic units of Bohr radii (a_0) and Hartrees (E_h) are the traditional units of length and energy (respectively) used by most *ab initio* quantum chemists when working with potential energy surfaces, although the spectroscopic units of Angstroms (Å) and wavenumbers (cm^{-1}) seems to be gaining popularity as the spectroscopy becomes increasingly pervasive. For consistency, atomic units will be used throughout the current discussion of the various potential energy surfaces.

The potential energy surfaces used herein for both H_2-Ar and H_2-Ne have been generated by starting with the Exchange Coulomb (`XC`) potential energy surface model which was then fine tuned by a fit to high resolution infrared spectroscopic, second virial coefficient and Raman pressure shifting data. This fine-tuned `XC` potential is referred to as an `XC(fit)` potential energy surface. In the case of H_2-He however, the Van der Waals attraction of this complex is so weak that spectroscopic data are unavailable. The potential energy surface for this system has been generated using the *ab initio* configuration interaction (CI) technique [16, 19]. As will be discussed shortly, these potential energy surfaces not only differ in the manner in which they have been generated, but also in the way that they have been documented. The potential energy surfaces for

H_2-Ar and H_2-Ne share a common lineage which allows a conjunctive discussion of their use in the present work. The potential energy surface for H_2-He will require a separate and more involved discussion to document the added work required to prepare this potential energy surface for this research.

3.2 The `XC(fit)` Potentials: H_2-Ar and H_2-Ne

The Exchange Coulomb (`XC`) model developed by Ng *et al.* is an *ab initio* potential energy surface originally designed to model the interaction of closed shell atom-atom systems [20, 21, 22], but has since been successfully adapted to diatom-noble gas systems such as N_2-Ar [23], N_2-Kr [24], CO-He [25], H_2-Ar [2] and H_2-Ne [18]. The `XC` model is simply defined as the sum of two terms: a short-range repulsive Heitler-London interaction term $E_{\mathrm{HL}}^{(1)}$, and a long range attractive induction/dispersion term $\Delta E_C(R,\theta,\xi)$, *viz.*

$$V(R,\theta,\xi) = E_{\mathrm{HL}}^{(1)} + \Delta E_C(R,\theta,\xi). \tag{3.2}$$

Where R represents the atom-diatom centre-of-mass separation, θ describes the relative orientation of the diatom bond relative to the atom, and $\xi = (r - r_0)/r_0$ is the dimensionless diatom bond stretching coordinate which is defined in terms of the diatom bond length r and its ground state equilibrium value r_0. This representation is often referred to as the `XC(0)` model to signify that it is purely *ab initio* and does not contain any empirical parameters. The `XC(0)` surface, while qualitatively correct, lacks the quantitative accuracy needed to model highly accurate modern experimental data such as that found in high resolution infrared spectra. To increase the flexibility of the `XC` model, an empirical scaling factor F is introduced to the Heitler-London term of the `XC(0)` surface and subsequently optimised using high resolution infrared spectral data, second virial coefficients, and Raman Q-branch line-shifting data. The resulting potential energy surface is called `XC(fit)` to signify that the *ab initio* `XC(0)` model has been fine-tuned by fitting the scaled model to accurate experimental data.

The analytical description of these `XC(fit)` potential energy surfaces means that `MOLSCAT` potential subroutines can be created immediately without having to conduct any time-consuming fitting procedures to transform the given potential into a more usable form. As can be seen by the amount of work needed to fit a tabulated potential energy surface analytically (as described in §3.3), the advantage of a potential energy surface already represented analytically is considerable. More time can be saved by adapting the pre-existing `MOLSCAT` potential subroutines for both H_2-Ar [2] and H_2-Ne [18] to suit the needs of the present research. The original subroutines are not designed to handle calculations involving vibrationally inelastic processes as required by the calculations found herein. However, a large majority of the code from these vibrationally *elastic* subroutines has been adapted to construct vibrationally *inelastic* versions. Using these adapted potential subroutines, scattering calculations can now be attempted. More details about the specifics of these calculations can be found in §3.4.

A battery of trial scattering calculations have demonstrated that the H_2-Ne `XC(fit)` potential energy surface shows no obvious problems; however, the same can not be said for the H_2-Ar surface. The low-energy ground vibrational state (vibrationally elastic) calculations of Bissonnette *et al.* [2] using the `XC(fit)` H_2-Ar potential energy surface were probably unable to detect a pathogenic potential *turn-over* located in the then inaccessible very small ($R < 1.0$ a_0) atom-diatom separation region. The present vibrationally inelastic calculations are much larger in scope than the previous calculations of Bissonnette *et al.* [2] and Crowell [18], and consequently are more likely to sample regions of the potential energy surface not previously tested. Figure 3.1 demonstrates the extent of the potential turn-over found with H_2-Ar. Each curve in this figure represents a cut through a vibrationally-averaged H_2-Ar potential energy subsurface where $r = r_0$ and $\theta = 0°$. These vibrationally-averaged potentials are heavily used in `MOLSCAT` and the pathological turn-overs they possess are causing `MOLSCAT` to fail. In its current state, the H_2-Ar potential energy surface can not reliably be used for the large basis set, high kinetic energy calculations that are required herein. Several *ad hoc* attempts to refit this repulsive wall region to a

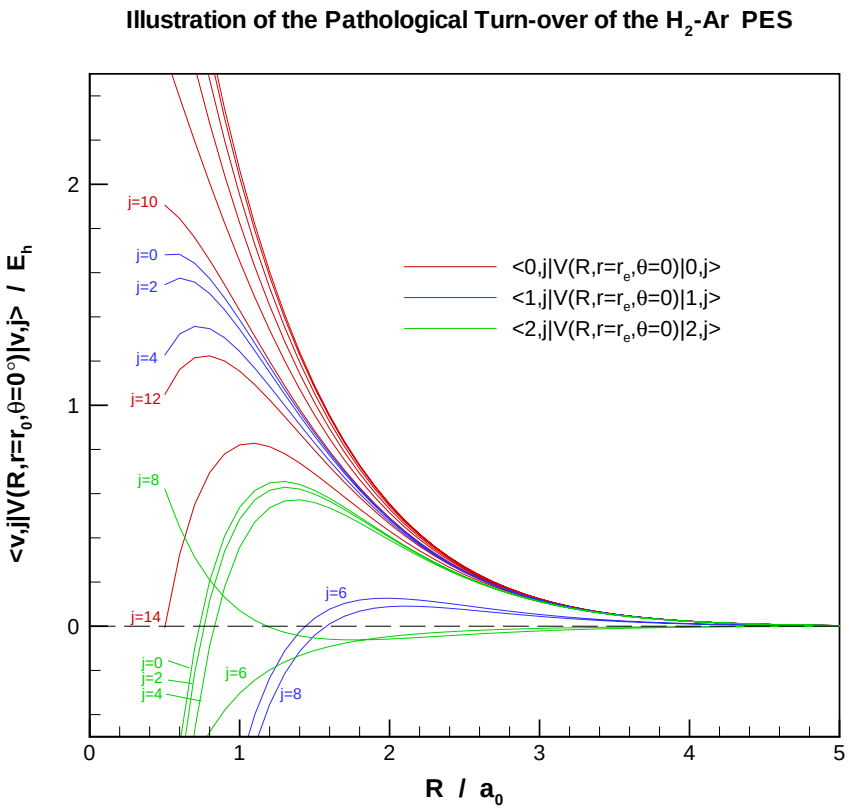

Figure 3.1: An illustration of the pathological short-range potential turn-over for H_2-Ar. Notice the number of vibrationally-averaged potentials which turn over for values of $R < 1.0$ a_0.

decaying exponential form have failed. Since a complete refit of the entire surface (with particular attention to the repulsive wall region) is beyond the scope of this work, a crude work-around will have to suffice. The turn-over has been removed by constraining each $V_\lambda(R, r)$ component of the surface at $R < 1.0$ a_0 to 100,000 E_h, a value indicative of the magnitude of the potential components in this region. This technique successfully removes the potential turn-over but introduces an artificial isotropic "plateau" for $R < 1.0$ a_0. The impact of this plateau on the scattering calculations should be minimal since it is energetically well separated from the present calculations.

3.3 The H_2-He Potential

As mentioned earlier, `XC(fit)` potential energy surfaces are generated by *ab initio* calculations and fine-tuned using the inversion of infrared spectral data, second virial coefficients, and Raman pressure shifting data [2]. In the case of H_2-He, spectroscopic data does not exist because the potential energy surface does not support any bound states. As a result, potential energy surfaces for H_2-He are developed from *ab initio* techniques. The potential energy surface that was chosen for this work is the three dimensional *ab initio* surface of Schaefer and Köhler [16]. This potential energy surface is a combination of two previously published *ab initio* potential energy surfaces of Meyer, Hariharan and Kutzelnigg [19]. It is believed that the Schaefer and Köhler potential energy surface is one of the most accurate and reliable surfaces with which to carry out vibrationally inelastic scattering calculations.

One major drawback to this potential energy surface is the tabular format with which it has been reported. From a computational perspective, this tabular format is quite inconvenient insofar as interpolation and extrapolation are concerned. Calculations using this potential energy surface can (and in fact, will almost exclusively) interrogate the surface between the tabulated points. Tabulated data can provide no information about nature of the data between or beyond the tabulated points. For this reason an external interpolation and extrapolation scheme will be required. However, interpolation and extrapolation schemes typically use arbitrary curves to connect the tabulated data in an aesthetically pleasing, yet non-physical manner. In contrast, if the tabulated potential energy surface were to be 'fitted' to an analytic form which is based (to some degree) on a physical model of the system at hand, the problems of interpolation and extrapolation become less troublesome. An analytic form based on a physical model of the system has built-in characteristics which provide a much more reliable ability to predict data between (or beyond) the tabulated points.

The quality of these fits can be assessed through the use of the quantity called the dimensionless

standard error (DSE) $\bar{\sigma}_f$,

$$\bar{\sigma}_f = \left\{ \frac{1}{N-M} \sum_{i=1}^{N} \left[\frac{y_{\mathrm{calc}}(i) - y_{\mathrm{obs}}(i)}{u(i)} \right]^2 \right\}^{1/2}, \tag{3.3}$$

where each of the N tabulated data points $y_{\mathrm{obs}}(i)$ has an uncertainty of $u(i)$, and $y_{\mathrm{calc}}(i)$ is the value of the datum i predicted by the M-parameter fit [26]. A fit in which the model represents the original data to a level consistent with the uncertainties of the original data will result in a DSE which is close to unity ($\bar{\sigma}_f \sim 1$). Fits which result in DSE's larger than unity represent poorer quality of fits, while fits which result in a DSE less than unity represent higher quality fits. The work of Schaefer and Köhler does not document any values for the uncertainties of the points that define their surface. Using the number of significant figures reported in the tabulated data as a guide, a modest artificial uncertainty of 1×10^{-6} E_h was assigned to each point on the surface. Due to the somewhat subjective choice for the uncertainties of the points in the tabulated data, the absolute value of the DSE is not as helpful as previously mentioned. Since the DSE is inversely related to the data uncertainty (3.3), a larger choice for the uncertainty of the points in the tabulated data will result in a smaller DSE, and vice versa. However, the relative values of the DSE between different fits performed using the same uncertainties will provide a method to gauge the *relative* "goodness" of the fits. It should be noted that for some cases, such as the problematic small atom-diatom separation region, some *ad hoc* manipulation of the artificial uncertainties can be imposed on the tabulated data to facilitate the fitting of the tabulated data in these regions.

3.3.1 The Diatom Bond Length Coordinate, r

Before discussing the details of the diatom bond length coordinate fitting procedure, it is instructive to mention the format that has been used to tabulate the Schaefer and Köhler potential energy surface. A common practise when it comes to describing the angular dependence of potentials possessing high levels of angular symmetry, such as that found in atom-homonuclear diatom

systems, is to incorporate the angular dependence of the potential into a Legendre series such as

$$V(R,r,\theta) = \sum_{\lambda=0,2}^{4} V_\lambda(R,r) P_\lambda(\cos\theta), \tag{3.4}$$

where $P_\lambda(\cos\theta)$ are the Legendre polynomials, and $V_\lambda(R,r)$ represent the potential component sub-surfaces corresponding to the angular symmetry of $P_\lambda(\cos\theta)$. Schaefer and Köhler have supplied their potential energy surface in terms of a set of five tables, each table representing a *slice* through each of these three potential component sub-surfaces $V_\lambda(R,r)$ for a given value of the diatom bond length (r=0.900, 1.280, 1.449, 1.618 and 2.000 a_0) as a function of atom-diatom separation R. Since the angular dependence of the potential energy surface has been incorporated by the Legendre series, this leaves only the diatom bond length r and the atom-diatom separation R coordinates to be fit. Ideally a multi-dimensional surface fitting procedure will be used to fit these last two degrees of freedom simultaneously, but such fitting procedures can be exceedingly difficult to configure and proof. To avoid the pitfalls associated with such surface fitting, two consecutive multi-dimensional curve-fitting procedures will be used. The first fitting procedure is responsible for the diatom bond length dependence while the second fitting procedure is responsible for the atom-diatom separation dependence of the potential energy surface. This sequential method of fitting the surface is not without its drawbacks. Depending on the tabulated potential energy data and the flexibility of the functional forms that are used in the fitting procedure this method may mistakenly find a *locally* optimised set of parameters instead of the true *globally* optimised values. This problem, which plagues almost all multi-dimensional non-linear least-squares fitting procedures, is slightly more problematic here because a poorly optimised parameter found in the first step will passed to the second step, which will further the damage. By varying the initial trial parameters the users can convince themselves that the optimised parameters found during the first step of the fitting procedure correspond to the *globally* optimised values, and then proceed to the second step of the process with confidence.

Returning to the diatom bond length fitting procedure, a power series in the dimensionless

stretching coordinate $\xi = (r - r_0)/r_0$ has been chosen to represent the diatom-bond length dependence of the potential energy surface,

$$V_\lambda(R,r) = \sum_{k=0}^{N} W_{\lambda k}(R)\xi^k = \sum_{k=0}^{N} W_{\lambda k}(R)\left(\frac{r-r_0}{r_0}\right)^k. \tag{3.5}$$

Where $W_{\lambda k}(R)$ are the coefficients of the fitted power series, and r_0 represents the equilibrium diatom bond length of H_2 in its ground rovibronic state ($r_0 = 1.449$ a_0). A power series was selected as the functional form for this fitting procedure for several reasons. The scattering calculations which comprise the bulk of the computational effort of this research will require a large number of matrix elements of the potential energy surface (2.6). Combining 3.4 and 3.5, these intramolecular matrix elements can be rewritten as

$$\mathsf{M}_{vj\to v'j'} = \langle\phi^{JM}_{vjl}(r,\theta)|V(R,r,\theta)|\phi^{JM}_{v'j'l'}(r,\theta)\rangle \tag{3.6}$$

$$= \sum_{k=0}^{2}\sum_{\lambda=0,2}^{4} W_{\lambda k}(R)\langle\phi^{JM}_{v''j''l''}(r,\theta)|\xi^k P_\lambda(\cos\theta)|\phi^{JM}_{vjl}(r,\theta)\rangle. \tag{3.7}$$

The angular portion of these matrix elements is readily soluble by `MOLSCAT` thanks to orthogonality and other properties of Legendre polynomials. The radial portion, however must be calculated externally and supplied to `MOLSCAT` along with the rest of the input data. These radial matrix elements can be calculated using the Le Roy `LEVEL 7.0` program [27] with the Schwartz-Le Roy H_2 potential energy function [28]. As will be seen below, the power series functional form has the added benefit of being a linear function with respect to its parameters, which permits a simple *linear* least-squares fitting procedure to be used.

The Schaefer-Köhler potential energy surface has only been evaluated at five different diatom bond lengths, which means that a four-term (or smaller) power series should be used to provide a reliable fit. Fitting data to analytic functions is somewhat of an art form, and great care must be used to minimise the number of parameters so as to create as compact a representation of the original data as possible without significantly decreasing the quality of the overall fit. The

linear least-squares fitting algorithm which has been used is the Le Roy linear least-squares fitting program called `llsqf` [29]. In this case, it was found that a three term power series ($N = 2$) generates a sufficiently compact representation of the Schaefer-Köhler data with a minor impact on the quality of the overall fit.

A total of 144 separate linear least-squares fits are needed to represent the diatom-bond length dependence of the potential energy surface. The overall potential energy surface has been partitioned into three sub-surfaces $V_0(R,r)$, $V_2(R,r)$ and $V_4(R,r)$ according to the Legendre expansion (3.4). Each of these sub-surfaces is tabulated at 48 different atom-diatom separations ranging from $R = 1.6$ a_0 to $R = 11.0$ a_0, creating 48 *slices* through each of these sub-surfaces. Every one of these 144 *slices* has been fit to a three-term power series, generating a total of 432 parameters. At small atom-diatom separations ($R \leq 2.4$ a_0) the fitting procedure faltered and produced fits with larger uncertainties. Despite these larger uncertainties the data points at small values of the atom-diatom separation have been shown to be an invaluable part of the potential energy surface, and must be included in the fitting procedure in order to prevent any pathological behaviour of the modified Lennard-Jones oscillator radial functions during the next step of the fitting procedure.

The next stage in the surface fitting process is to take the fitted parameters $W_{\lambda k}(R)$ with their uncertainties and fit the remaining atom-diatom separation dependence of the overall PES to the modified Lennard-Jones (12,6) oscillator functional form. As will be shown in the following section, the modified Lennard-Jones (12,6) oscillator function has sufficient flexibility to incorporate the long range $C_6^{\lambda,k}$ dispersion coefficients which have been carefully calculated by Thakkar *et al.* [30].

3.3.2 The MLJ and the Atom-Diatom Separation Coordinate, R

The Van der Waals force is the dominant interaction in H_2-Ng systems (Ng = {He,Ne,Ar...}). It is also the dominant interaction in noble gas dimer (Ng_2) systems. In the 1930's and up until the mid 1960's the Lennard-Jones ($2n$,n) potential energy function (equation 3.8) was considered to

be an adequate potential energy function for describing these types of weakly interacting Van der Waals systems [31]. The standard Lennard-Jones (12,6) function can be represented as

$$V_{\mathrm{LJ}}(R) = D_e \left[1 - \left(\frac{R_e}{R}\right)^n\right]^2 - D_e, \tag{3.8}$$

where D_e is the well depth at the equilibrium bond distance R_e. The value of n will determine the type of Lennard-Jones potential energy functions, for example if $n = 6$ (as is the case herein) the familiar Lennard-Jones (12,6) potential energy curve is produced. The Lennard-Jones ($2n$,n) potential energy function has long since been replaced by more sophisticated and accurate potential energy functions. However with a few modifications the usefulness of the Lennard-Jones potential energy functional form can be revitalized to a certain extent. In 2000, Hajigeorgiou *et al.* introduced a new variation on the Lennard-Jones potential energy function called the modified Lennard-Jones (MLJ) oscillator function [32],

$$V_{\mathrm{MLJ}}(R) = D_e \left[1 - \left(\frac{R_e}{R}\right)^n e^{-\beta(z)z}\right]^2 - D_e, \tag{3.9}$$

where

$$\beta(z) = \sum_{m=0}^{N} \beta_m z^m, \tag{3.10}$$

and $z = (R - R_e)/(R + R_e)$. This potential energy function, like its predecessor, has a form which readily permits it to be constrained to an inverse-power form at large values of R. In the long range, $R \to \infty$ and $z \to 1$ which will make the beta function collapse to a sum of its coefficients (referred to as β_∞)

$$\beta_\infty = \lim_{z \to 1} \beta(z) = \sum_{m=0}^{N} \beta_m. \tag{3.11}$$

The long range form of the MLJ potential function can now be written as the familiar inverse-power relationship,

$$\lim_{R \to \infty} V_{\mathrm{MLJ}}(R) = -2D_e \left(\frac{R_e}{R}\right)^n e^{-\beta_\infty} = -\frac{C_n}{R^n}, \tag{3.12}$$

where

$$C_n = 2D_e R_e^n e^{-\beta\infty}. \tag{3.13}$$

It should be noted that the MLJ potential energy function was designed to handle potential energy curves, not necessarily $W_{\lambda k}(R)$ potential energy components *per se*. Potential energy components usually exhibit potential curve-like properties such as repulsive walls, attractive long range tails and potential wells, but there are no guarantees that these features will be found in the $W_{\lambda k}(R)$ potential components. For the most part it is expected that the MLJ (12,6) potential energy function will describe the $W_{\lambda k}(R)$ potential component functions reliably, but it should be expected that some of these potential component functions may require some additional attention in order to facilitate the fitting procedure. Based on the previous successes of the MLJ potential energy function demonstrated by Hajigeorgiou and Le Roy [32] and its convenient inverse-power long range form, the modified Lennard-Jones (12,6) potential energy function has been chosen to represent the atom-diatom separation dependence of the tabulated potential energy surface.

The atom-diatom separation dependence of the potential energy surface is the only coordinate which still requires analytical representation. Equation 3.5 demonstrates that the atom-diatom separation coordinate appears only in the coefficients $W_{\lambda k}(R)$ of the power series expansion. These coefficients and their uncertainties generated during the diatom bond length fitting procedure, in conjunction with the long range $C_6^{\lambda,k}$ dispersion coefficients of Thakkar *et al.* [30], can now be fitted to the modified Lennard-Jones (12,6) oscillator function. In contrast to the linear least-squares procedure used to fit the diatom bond length dependence to a power series expansion, a non-linear least square fitting procedure is required to fit the atom-diatom separation dependence to the modified Lennard-Jones (12,6) oscillator function. A non-linear least-squares fitting procedure is required whenever the fitting function does not depend linearly upon its parameters [33]. This (non-)linearity can be demonstrated by examining the partial derivatives of the fitting function with respect to its parameters. For example, the diatom bond length fitting procedure involved a three-term power series fitting function, (Equation 3.5). The partial derivatives of this

power series with respect to the parameters $W_{\lambda k}(R)$ are,

$$\frac{\partial V_\lambda(R,r)}{\partial W_{\lambda k}} = \xi^k, \tag{3.14}$$

which do not depend on the values of any of the $W_{\lambda k}$ parameters. This means that the power series functional form depends linearly upon its parameters, and consequently a linear least-squares fitting procedure is sufficient. However, the atom-diatom separation dependence of the potential energy surface is to be fit to the modified Lennard-Jones (12,6) fitting function,

$$W_{\lambda k}(R) = D_e \left[1 - \left(\frac{R_e}{R}\right)^6 e^{-\beta(z)z}\right]^2 - D_e \tag{3.15}$$

where by combining 3.11, and 3.13,

$$\beta(z) = \sum_{m=0}^{N-1} \beta_m (z^m - z^N) + \ln\left(\frac{2D_e R_e^6}{C_6^{\lambda,k}}\right) z^N. \tag{3.16}$$

The partial derivatives of this fitting function with respect to its parameters $(D_e, R_e, \{\beta_i\}, C_6^{\lambda,k})$ are given by

$$\begin{aligned}
\frac{\partial W_{\lambda k}(R)}{\partial D_e} &= 2z^{N+1}\left(\frac{R_e}{R}\right)^6 e^{-\beta(z)z}\left[1 - \left(\frac{R_e}{R}\right)^6 e^{-\beta(z)z}\right] \qquad (3.17)\\
&\quad + \left[1 - \left(\frac{R_e}{R}\right)^6 e^{-\beta(z)z}\right]^2 - 1,\\
\frac{\partial W_{\lambda k}(R)}{\partial R_e} &= -2D_e\left(\frac{R_e}{R}\right)^6 e^{-\beta(z)z}\left[1 - \left(\frac{R_e}{R}\right)^6 e^{-\beta(z)z}\right]\left[\frac{6}{R_e}(1 - z^{N+1})\right. \qquad (3.18)\\
&\quad \left. + \frac{4R^2(N+1)}{(R+R_e)^4}\left(\sum_{m=0}^{N-1}(m+1)\beta_m z^m\right)\ln\left(\frac{2D_e R_e^6}{C_6^{\lambda,k}}\right) z^N\right],\\
\frac{\partial W_{\lambda k}(R)}{\partial \beta_i} &= 2D_e\left[1 - \left(\frac{R_e}{R}\right)^6 e^{-\beta(z)z}\right]\left(\frac{R_e}{R}\right)^6 e^{-\beta(z)z}(z^{i+1} - z^{N+1}), \qquad i < N \qquad (3.19)\\
\frac{\partial W_{\lambda k}(R)}{\partial C_6^{\lambda,k}} &= \frac{-2D_e}{C_6^{\lambda,k}}\left[1 - \left(\frac{R_e}{R}\right)^6 e^{-\beta(z)z}\right]\left(\frac{R_e}{R}\right)^6 e^{-\beta(z)z} z^{N+1}. \qquad (3.20)
\end{aligned}$$

Each of these partial derivatives has an explicit dependence upon some or all of the parameters. This implies that the modified Lennard-Jones (12,6) functional form does *not* depend linearly upon its parameters, and hence a *non-linear* least-squares fitting procedure is required. These partial derivatives of the fitting function with respect to its parameters are important to the fitting process because it is these partial derivatives which serve to "navigate" the fitting algorithm through parameter space in search of the set of parameters which minimises $\bar{\sigma}_f$, the dimensionless standard error (DSE). In linear least-squares fitting procedures the parameter-independent partial derivatives permit a single-step simultaneous optimisation of all parameters. However, for non-linear least-squares procedures in which the partial derivatives depend on some or all of the parameters, an iterative algorithm is required to optimise all of the parameters using a variable step-size gradient search-type method. The non-linear least-squares fitting algorithm `nllssrr` of Le Roy [26] has been used for all non-linear least squares fits calculated herein.

The diatom bond length fitting procedure has generated nine distinct potential component functions $W_{\lambda k}(R)$ where $\lambda = \{0, 2, 4\}$ and $k = \{0, 1, 2\}$. Each of these functions is defined at 48 differents atom-diatom separations ranging from $R = 1.6$ a_0 to $R = 11.0$ a_0. Instead of allowing the fitting procedure to vary the long range $C_6^{\lambda,k}$ dispersion coefficient parameters, these coefficients are fixed using the *ab initio* $C_6^{\lambda,k}$ coefficients calculated by Thakkar *et al.* [30]. These parameters, henceforth referred to as constants, are removed from the fitting procedure. Hereto unaddressed has been the number of parameters defining the beta function. As discussed earlier, the goal when fitting data to analytical forms is to minimise the number of parameters without introducing any significant negative impact to the quality of the fit. The number of parameters in the beta function was determined by comparing a series of different fits having different numbers of parameters. When the optimised value of the n-th parameter became smaller than its uncertainty, the beta function $\beta(z)$ was terminated at the $(n-1)$-th term. When a parameter value is overshadowed by its uncertainty, the fit is said to be insensitive to this parameter. Removing an insensitive parameter from the fit will typically only produce a minor impact on the overall quality of the fit. For the most part it was found, using this technique, that a three-parameter

$\{\beta_0, \beta_1, \beta_2\}$ beta function was sufficient.

During the fitting procedure it became clear that certain potential component functions $W_{\lambda k}(R)$ could not be represented by a modified Lennard-Jones (12,6) oscillator function. Originally it was hoped that all nine potential component functions could be expressed by nine separate modified Lennard-Jones (12,6) oscillator functions containing the same number and configuration of parameters. Such a representation is aesthetically pleasing, as well as making computer programming tasks slightly more manageable. Unfortunately, the current form of the modified Lennard-Jones (12,6) oscillator function can not be successfully fit to four of the nine potential energy components: $W_{02}(R)$ and all of the $W_{4k}(R)$ components. Non-linear fitting procedures require a great deal of human intervention in order to work properly. The choice of the initial trial parameters, the data uncertainty and model flexibility all combine to determine whether or not a fit will converge or not. Model flexibility is something that can't be changed without changing the model, but the choice of the initial trial parameters and the data uncertainty are things which can be changed in order to help improve the success of a model in representing the data as accurately as possible. Many different sets of initial trial parameters were unsuccessful in generating a useable fit of the tabulated data to the modified Lennard-Jones (12,6) oscillator function. In addition, several *ad hoc* manipulations of the input data uncertainties were also unable to help produce useable fits. Almost the only recourse left was to adapt the model.

The $W_{02}(R)$ Potential Component Function

In the case of the $W_{02}(R)$ potential component, the problem is found to be that the long range behaviour of the model, described by the $C_6^{\lambda,k}$ dispersion coefficient, does not resemble the long range data. This potential component possesses a primary well-like feature at $R \sim 2.2$ a_0, a barrier-like feature at $R \sim 4.0$ a_0 and a very shallow secondary well-like feature at $R \sim 8.8$ a_0. The secondary well cannot be modelled by a Lennard-Jones-like potential energy function. However, the barrier-like feature *can* be duplicated by a MLJ (12,6) potential energy function

if the fitting procedure is allowed to vary the parameters of the model beyond their physically reasonable limits. A barrier can be produced by allowing D_e, the well-depth (usually a positive quantity) to become negative (now representing a barrier height), and forcing the MLJ (12,6) oscillator function to model the primary well using the otherwise-pathological potential turn–over behaviour. While the barrier can be modelled particularly accurately using this method, the primary well is very poorly represented. It is believed that the manifestations of the second well and the barrier are minor relative to the other features present on the potential component function, such as the repulsive wall, primary well and attractive long range tail. The barrier and secondary well occur at relatively large atom-diatom separation distances where the $C_6^{0,2}$ dispersion coefficient parameter is becoming dominant. Because these features do not correlate with the inverse power model of the long range behaviour of the fitting function, the fitting procedure fails. In order to increase the flexibility of the model, the $C_6^{0,2}$ dispersion coefficient constraint was removed from this fit and the data uncertainty was modestly increased in the regions of the barrier and secondary well features. With this added flexibility $W_{02}(R)$ can be fitted using three β_m parameters. Figure 3.2C demonstrates the unusual shape of the $W_{02}(R)$ potential component and the best fit MLJ (12,6) function that could be found.

The $W_{4k}(R)$ Potential Component Functions

The $W_{4k}(R)$ potential components functions are undeniably the most disappointing results from this fitting procedure. All of the $W_{4k}(R)$ components exhibit very unusual features which made fitting them to MLJ (12,6) oscillator functions exceedingly difficult. For example, the $W_{40}(R)$ potential component has no significant well-like feature, the $W_{41}(R)$ component has a very broad and shallow well-like feature located at a large distance $R \sim 9.5$ a_0, and the $W_{42}(R)$ component possesses an extremely shallow well-like feature centred at $R \sim 7.4$ a_0 followed by a short barrier-like feature at $R \sim 9$ a_0. In addition there are several oddly-shaped kinks and bends in the repulsive wall of each of these potential components, becoming progressively more dramatic as k increases. It became clear after dozens of failed fitting attempts that the MLJ (12,6) oscillator functions were just not flexible enough to represent these potential components, and that another

fitting function was required. Undoubtedly, experts in the fields of data reduction and non-linear fitting have tried and true methods for selecting appropriate fitting functions based on the data at hand and the flexibility of various different functional forms. Without expert guidance the only option available was to *cut and try* different combinations of functional forms until a usable fitting function is found. This is an extremely painstaking process. For each new combination of functional forms, a new set of partial derivatives are required, and a considerable amount of time must be spent massaging the initial trial parameters. The functional form which seemed to provide the best results was found by selectively removing various components from the MLJ (12,6) oscillator function, leaving

$$W_{4k}(R) = \mathcal{D}_e \exp(-\mathcal{B}(z)), \tag{3.21}$$

where

$$\mathcal{B}(z) = \sum_{m=1}^{\mathcal{N}} \mathcal{B}_m z^m, \tag{3.22}$$

and $z = (R - \mathcal{R}_e)/(R + \mathcal{R}_e)$. The parameters in this functional form do not have the same meaning as their respective equivalents in the MLJ (12,6) oscillator form. However, since all of the parameters are derived from the MLJ (12,6) parameters they have been named to reflect the parameter to which they are most closely related. This functional form, like the MLJ (12,6) oscillator functions, depends non-linearly upon its parameters, and hence will require the Le Roy `nllssrr` program to carry out the non-linear least-squares fitting. The partial derivatives of this exponential function with respect to its parameters are:

$$\frac{\partial W_{4k}(R)}{\partial \mathcal{D}_e} = \exp\left(-\mathcal{B}(z)\right), \tag{3.23}$$

$$\frac{\partial W_{4k}(R)}{\partial \mathcal{R}_e} = \frac{2\mathcal{D}_e R}{(R + \mathcal{R}_e)(R - \mathcal{R}_e)} \left(\sum_{m=1}^{\mathcal{N}} \mathcal{B}_m m z^m \right) \exp(-\mathcal{B}(z)), \tag{3.24}$$

$$\frac{\partial W_{4k}(R)}{\partial \mathcal{B}_i} = -\mathcal{D}_e z^i \exp(-\mathcal{B}(z). \tag{3.25}$$

The best fits using this exponential fitting function were achieved with the $\mathcal{R}_e$ parameter fixed at $\mathcal{R}_e = 2.00000$ a_0 or 3.00000 a_0 For the $W_{40}(R)$ and $W_{42}(R)$ potential components three $\mathcal{B}_m$ parameters were needed, while $W_{41}(R)$ only required two. It is unclear why $\mathcal{R}_e$-constrained fits would provide better results than wholly unconstrained fits; in addition, the special significance of $\mathcal{R}_e = 2.000000$ a_0 and $\mathcal{R}_e = 3.000000$ a_0 is a mystery. Perhaps with more experience a better fitting function could be chosen for these potential components, but for the time being this exponential fitting function is the best form available. Despite the mysteriousness of the constrained $\mathcal{R}_e$ values, the troublesome $W_{4k}(R)$ potential component functions have been fit to analytic functions. As shown in figure 3.4 the fits are far from perfect, but given the fact that the unfittable features are very small relative to the other features in each potential component, it is hoped that these unfittable features are of minor importance to the overall potential energy surface.

Combined, all nine potential component functions $W_{\lambda k}(R)$ form the analytical representation of the tabulated Schaefer and Köhler potential energy surface. The optimised parameters corresponding to the best fit of the potential energy surface can be found in Appendix A tables A.1 and A.2. Before proceeding to any calculations using the newly fitted version of the potential energy surface, it should be tested against the original tabulated data. Ideally, the fitted surface and the tabulated surface should be identical, but since some of the features in the $W_{02}(R)$ and $W_{4k}(R)$ potential components could not be fully modelled by the fitting functions, the fitted and tabulated potential energy surfaces will be slightly different. To gauge this difference, a point-by-point comparison of the two surfaces is needed.

The original tabulated potential energy surface consists of 240 data points. The fitted potential can be evaluated to recreate these 240 points for the point-by-point analysis of the two surfaces. Figure 3.5 illustrates such a point-by-point absolute difference between the original tabulated form of the potential and the newly fitted version. The components $V_\lambda(R, r)$ shown in this figure correspond to the previously mentioned *slices* of the original tabulated potential energy surface for a given $\lambda = \{0, 2, 4\}$ and $r = \{0.900, 1.280, 1.449, 1.618, 2.000\ a_0\}$. The largest

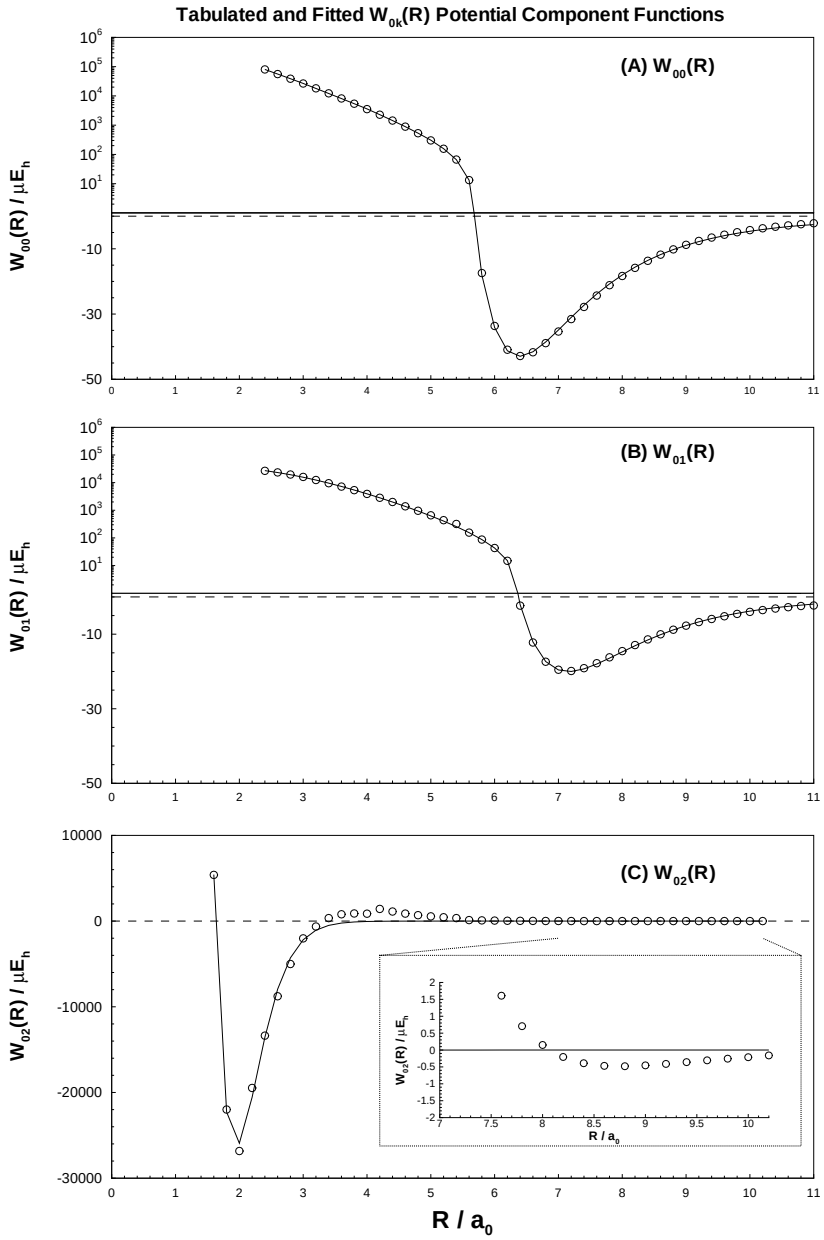

Figure 3.2: The $W_{0k}(R)$ potential components. The ∘ symbols represent the tabulated data of Schaefer and Köhler, while the line represents the corresponding fitted MLJ (12,6) oscillator function. **(A)** illustrates the $W_{00}(R)$ potential component, **(B)** illustrates the $W_{01}(R)$ potential component and **(C)** illustrates the $W_{02}(R)$ potential component.

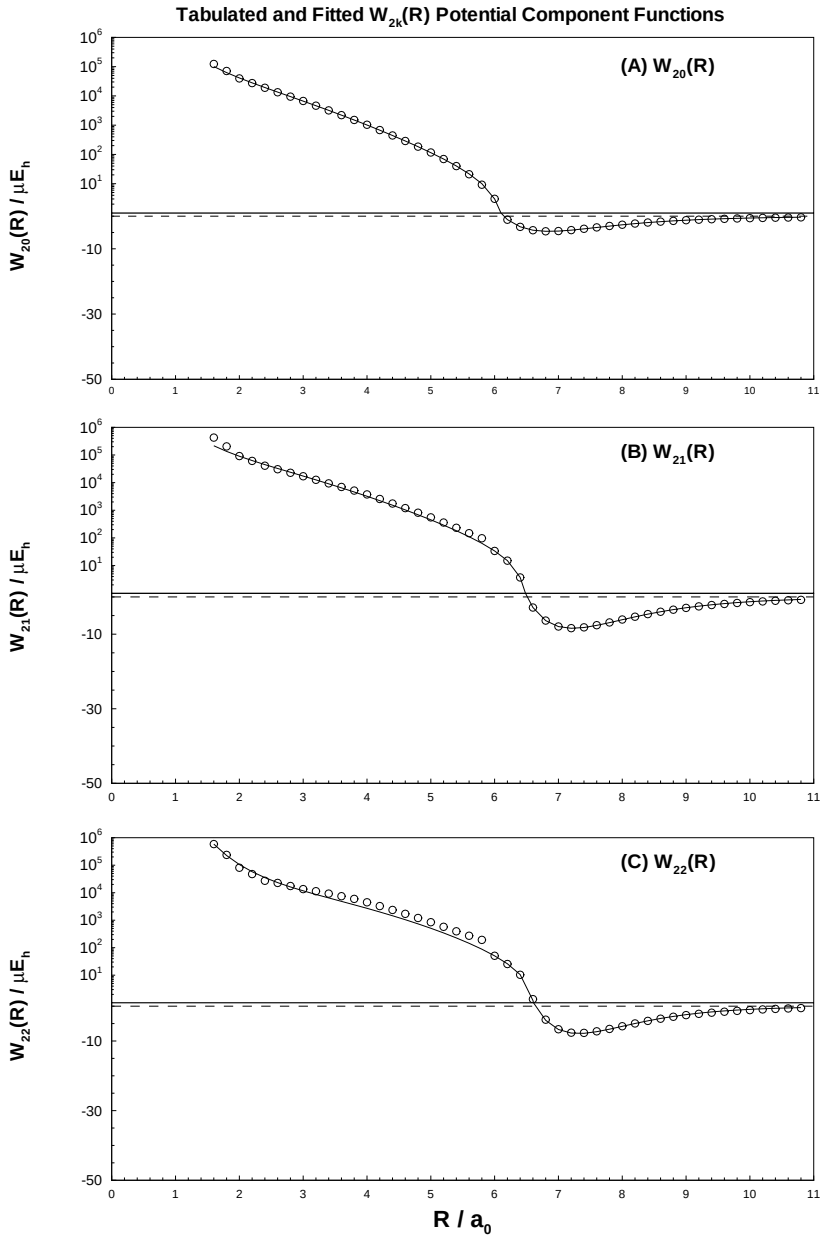

Figure 3.3: The $W_{2k}(R)$ potential components. The ∘ symbols represent the tabulated data of Schaefer and Köhler, while the line represents the corresponding fitted MLJ (12,6) oscillator function. **(A)** illustrates the $W_{20}(R)$ potential component, **(B)** illustrates the $W_{21}(R)$ potential component and **(C)** illustrates the $W_{22}(R)$ potential component.

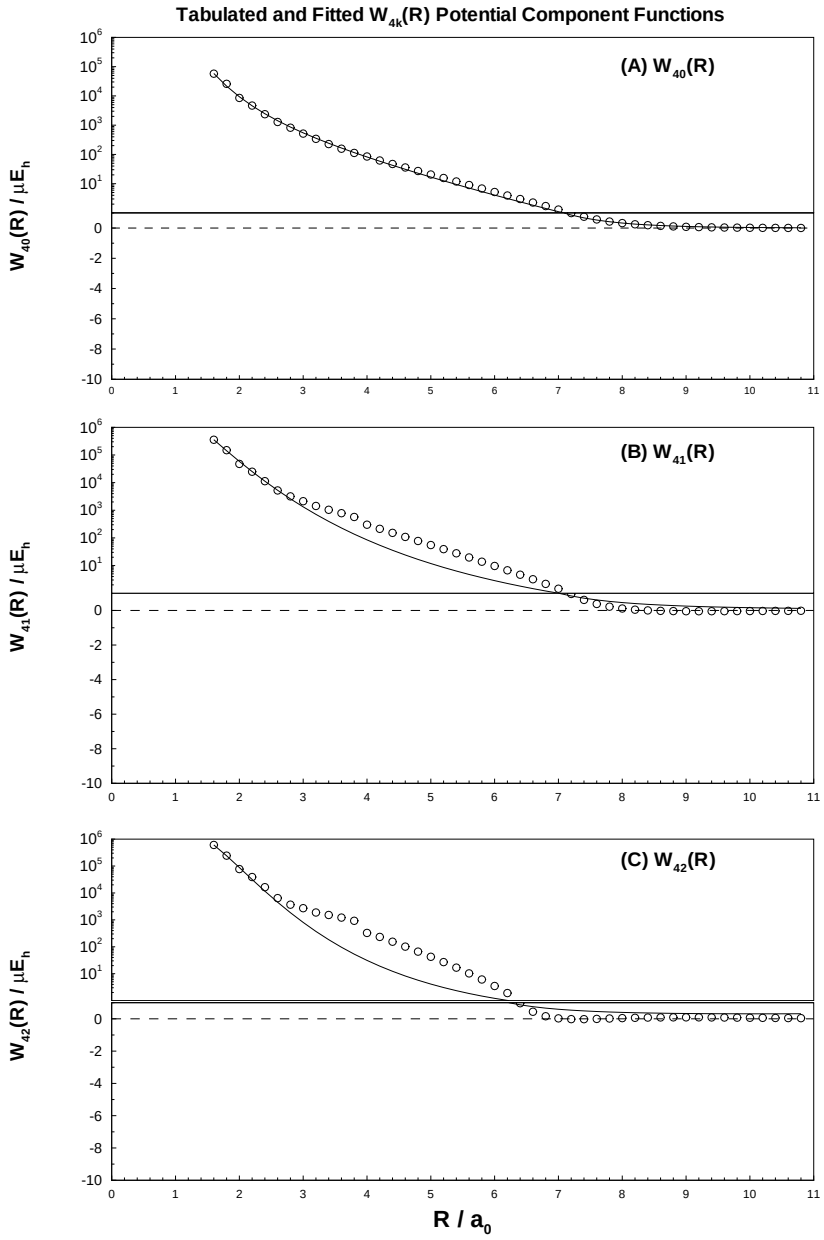

Figure 3.4: The $W_{4k}(R)$ potential components. The ∘ symbols represent the tabulated data of Schaefer and Köhler, while the line represents the corresponding fitted MLJ (12,6) oscillator function. **(A)** illustrates the $W_{40}(R)$ potential component, **(B)** illustrates the $W_{41}(R)$ potential component and **(C)** illustrates the $W_{42}(R)$ potential component.

discrepancies of ~ 0.05 E_h are shown on the $V_2(R, 0.900)$ and $V_2(R, 2.000)$ components at small atom-diatom separations where the value of these potential components is only ~ 0.04 E_h and ~ 0.37 E_h, respectively. The corresponding deviation of these two components relative to their tabulated counterparts is a disturbing 125% and a tolerable 13%, respectively. However, these potential components only represent a small fraction of the total potential energy surface and by comparing these seemingly large discrepancies to the value of the total potential energy, the actual impact on the potential energy is much smaller at 9% and 5% respectively. These numbers represent the worst discrepancy between the fitted and tabulated potential components, and since there are three such symmetry components which define the entire potential energy surface, the worst-case error estimate for the repulsive wall of the potential is up to 27% error.

Better agreement is found in the well region of the potential energy surface $R \sim 6.4$ a_0. The fitted potential energy surface is more reliable here, with potential component deviations ranging from $\sim 2 \times 10^{-8} - 2 \times 10^{-6}$ E_h. The $V_\lambda(R, r)$ tabulated potential components are much smaller in this region $\sim 3 \times 10^{-5}$ E_h, which means these discrepancies correspond to 0.1-7% deviation. In comparison to the value of the total potential energy surface, which is also $\sim 3 \times 10^{-5}$ E_h, these deviations result in a worst-case error estimate in the well region of the total potential energy surface of up to 21% error. These numbers are large, but it must be stressed that they represent the absolute worst case in which the errors from each of the $V_\lambda(R, r)$ components share the same sign, creating the largest possible error. In reality, the sign of the errors from each potential component need not be the same and the positive and negative errors from the various components can cancel to yield a net error which is smaller than the errors quoted here.

Figure 3.5 illustrates the spatial distribution of the error between the fitted and tabulated potential energy surface, but it does not give a good indication of the quality of the fitted potential energy surface as a whole. The percent error between the fitted and tabulated versions of the

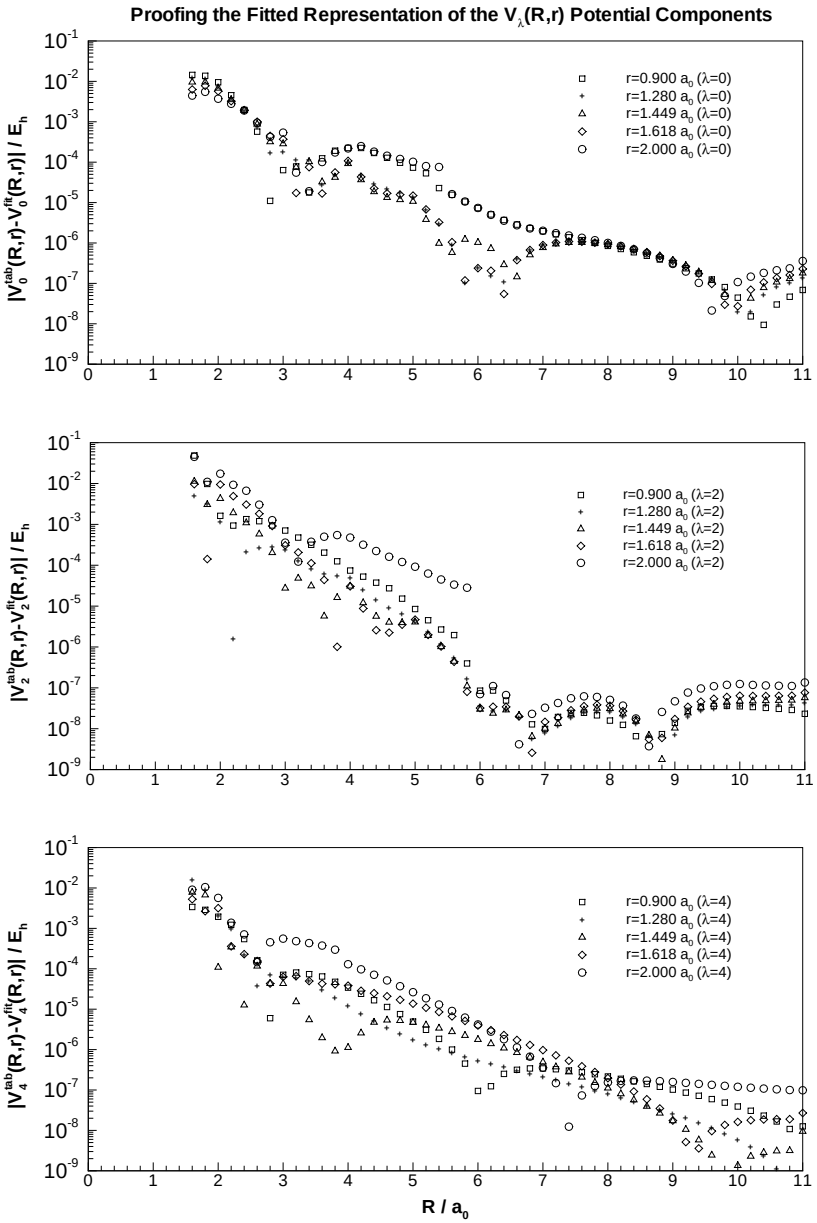

Figure 3.5: The absolute difference between the previously tabulated and newly fitted versions of the potential energy surface for each of the three symmetry components $\lambda = \{0, 2, 4\}$ at each of the five diatom bond length slices, $r = \{0.900, 1.280, 1.449, 1.618, 2.000\ \mathrm{a_0}\}$.

potential energy surface can be evaluated using,

$$\%\text{error} = \frac{|V_\lambda^{\text{fit}}(R,r) - V_\lambda^{\text{tab}}(R,r)|}{V_\lambda^{\text{tab}}(R,r)} \times 100. \tag{3.26}$$

Figure 3.6 presents a histogram of these point-by-point percent errors. Each bar represents the number of data points (percentage of the total number of data points) whose error lies in the interval $[x, (x+\delta x)]\%$. The width of each of these bars (also called *bins*) is $\delta x = 1\%$ except for the right-most bin which represents all errors greater than 40%. The $\circ$ symbols represent the accumulated number of data points (also in percentage of the total number of data points) whose error lie in the interval $[0, x]\%$. This figure illustrates that $\sim 75\%$ of 240 data points possess an error of less than 6%, and that 90% of the 240 data points possess an error of less than 12%. This shows that a vast majority of the potential energy surface is adequately modelled, and that the problematic points are relatively few in number. For completeness it should be mentioned that the $\sim 3\%$ of data points which possess errors greater than 40% is mostly artificial. Whenever the denominator of equation 3.26 becomes vanishly small the value of the percent error will correspondingly become very large. The potential energy surface is defined such that $V(R \to \infty, r, \theta) = 0$. Under this convention each potential component may possess a root where repulsive wall meets the potential well. At these roots the percent error is artificially enlarged, generating most of the data points which possess errors greater than 40%.

Generally speaking, the fitting procedure has been a success. The disagreements shown at small atom-diatom separations for all $V_\lambda(R,r)$ are disappointingly large, but not fatal. At small atom-diatom separations, where the fitted potential has some of the largest discrepancies, the value of the full tabulated potential energy surface is very large, e.g., $V(1.6\ \text{a}_0, r, \theta) \sim 0.5\ \text{E}_h$. These energies are so large that the scattering calculations, at kinetic energies between 0.01-0.05 E_h, are anticipated to be relatively insensitive to these problematic regions of the potential energy surface. It is naive to expect that any subsequent calculations involving this fitted version of the potential energy surface to be completely insensitive to the errors that the fitting procedure has introduced. However, before condemning the fitting procedure, a closer look at the entire

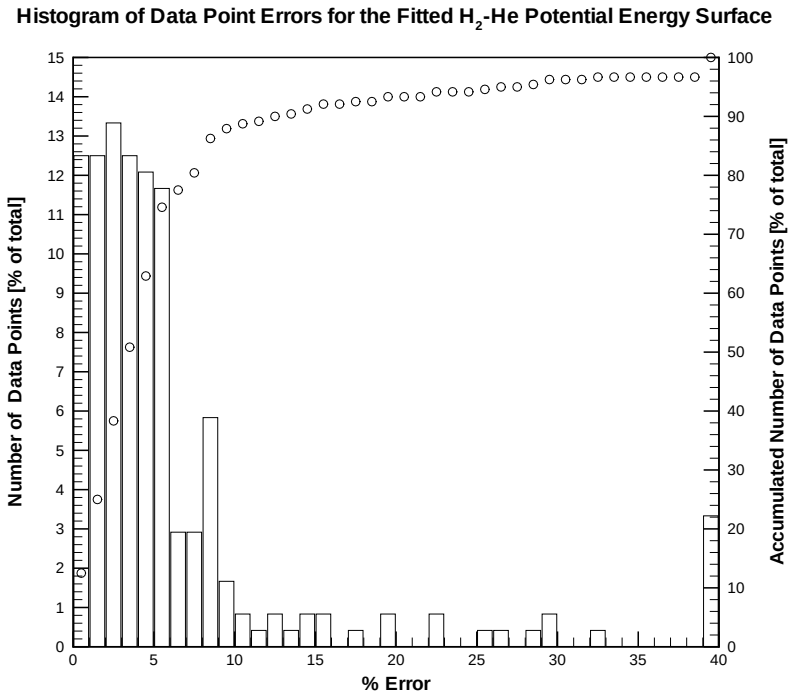

Figure 3.6: A histogram of the point-by-point percent errors of the fitted H_2-He potential energy surface. The bars represent the number of data points (in percent of the total number of data points) which possess an error in the interval $[x, (x+1)]\%$. The $\circ$ symbols represent the accumulated number of data points (in percent of the total number of data points) which possess an error in the interval $[0, x]\%$.

problem is in order. The tabulated potential energy surface data can not be directly incorporated into any calculation without introducing some mechanism to interrogate the surface between (and beyond) the tabulated points. Whether this mechanism is based on interpolation and extrapolation methods or a fitted analytical representation, the original tabulated data is only used to synthesize an artificial version of the potential energy surface for the calculations. Without being able to conduct calculations on the tabulated potential directly, it is impossible to determine the impact of these mechanisms on the subsequent calculations. Regardless of the mechanism used to generate the synthetic potential energy surface, the fact that synthetic potential energy surfaces *must* be generated indicates that misrepresentation errors are inevitable.

3.4 MOLSCAT

The general purpose inelastic molecular scattering program `MOLSCAT` by Hutson and Green [12] was used for all of the present scattering calculations. It is configurable, flexible and familiar, making it the best choice for the calculations at hand. `HIBRIDON`^{TM}, another general purpose inelastic molecular scattering program by Alexander *et al.* [13], was unable to be successfully built on any of the SGI research computers available, thereby eliminating its candidacy. All of the `MOLSCAT` calculations have been carried out using one of two separate computers: an SGI Origin 200 (dual tower) [34] with 270 MHz MIPS R12000 processors and MIPS R12010 FPUs, and an SGI Origin 2000 (deskside) [35] with 250 MHz MIPS R10000 processors and MIPS R10010 FPUs. Using these machines a scattering calculation takes between 15 and 90 minutes, depending on the size of the basis set and the kinetic energy.

A detailed description of the numerical solution to the close coupling equations is beyond the scope of this work, and has been previously detailed by Hutson [36], Gordon [37], Dunker and Gordon [38], Johnson [39] and Shapiro and Balint-Kurti [40]. In its place, a terse but informative description of some of the inner workings of `MOLSCAT` is supplied so as to give the reader a better feel for the decision-making process involved in the configuration of the scattering calculations

presented here. From this point forth, the natural units of molecular scattering will be used. Distances are conveniently expressed in terms of Angstroms (Å) while energies are expressed in terms of wavenumbers (cm^{-1}). The relationship between atomic units, which have been exclusively used thus far, and the scattering units is

$$\begin{aligned} 1\ a_0 &= 0.5291772083\ \text{Å}. \\ 1\ E_h &= 219,474.6315\ cm^{-1}. \end{aligned}$$

With a thorough discussion of the importance of the potential energy surface completed in the previous sections, it is now time to expound upon other important aspects of the scattering calculations, such as basis set convergence, convergence of the other input parameters, and the choice of propagator.

3.4.1 The Scattering Basis Set

Mathematically, a basis set is a collection of objects which, when assembled in different linear combinations, can span the entire object-space. Basis sets can be comprised of vectors, functions or, as is the present case, quantum states. In the present context, a basis set is defined as a collection of isolated H_2 molecular quantum states representing all of the diatomic states significantly involved in the scattering process. These basis states dictate the size and labelling of the most important entity in scattering theory: the S-matrix. Given the importance of the selection of the basis set, it is not suprising that the accuracy of the solutions to the close coupling equations will be directly related to the size and composition of the basis set. Accurate calculations require that all energetically accessible diatom quantum states must be present in the basis set. Additionally, several low-lying energetically inaccessible diatom quantum states must be included to ensure the completeness of the basis set. The larger the basis set is, the more complete the description of the scattering problem, and the more accurate scattering calculations will be. As the energy of the individual basis state become increasingly distant (relative to the scattering

v	j	Energy in cm^{-1}	Included in basis set ?
0	0	0.000	$\surd$
0	2	354.374	$\surd$
0	4	1168.798	$\surd$
0	6	2414.897	$\surd$
0	8	4051.943	$\surd$
1	0	4161.147	$\surd$
1	2	4497.820	$\surd$
1	4	5271.364	$\surd$
0	10	6030.919	
1	6	6454.376	
1	8	8007.573	
0	12	8298.597	

Table 3.1: The "rule of thumb" basis set from rotational relaxation calculations, naively extended into vibrational relaxation calculations.

energy), their involvement in the scattering process typically becomes increasingly insignificant. This allows the basis set to be truncated when the user is satisified that the omitted high energy diatomic states are not significantly relevant to the scattering problem at hand. The higher accuracy gained by use of a larger basis set is obviously more favourable than the reduced accuracy obtainable from a smaller basis set. However there is more to consider than just the calculational accuracy. Large basis sets beget large S-matrices, and the computational effort required to solve such problems can be formidable. A balance must be struck between having slower more accurate calculations using a large basis set, and quicker less accurate calculations using a smaller basis set.

The basis set selection begins by investigating the basis sets used for previous $v = 0$ rotationally inelastic scattering calculations, such as the standard basis set as described by Clark [41]. In his work, Clark describes a "rule of thumb" method where all energetically accessible diatomic molecular states plus the $2j + 1$ degenerate states of the next highest molecular energy level are included in his basis set. This is a standard method for selecting a basis set for $v = 0$ rotationally inelastic scattering problems. Now consider the basis set for a vibrationally inelastic scattering calculation at $E = 5000\,\mathrm{cm}^{-1}$, according to this "rule of thumb" criteria. Table 3.1 shows a few of the low-lying rovibrational states of *para*-H_2. In the $v = 0$ vibrational manifold, the $j = 0, 2, 4, 6,$

and 8 rotational levels are energetically accessible, as well as the $j = 0$ and 2 rotational levels in the $v = 1$ manifold. The $j = 4$ rotational level in the $v = 1$ vibrational manifold is also included in this basis set as the first energetically inaccessible level.

For the sake of simplicity, a more compact representation of the rovibrational levels in the basis set is needed. The basis set notation $\{j_0, j_1, j_2, \cdots, j_n\}$ represents the maximum values of the rotational quantum numbers in each vibrational manifold. Using this notation implies that all rotational levels in the interval $[0, j_i]$ for the i-th vibrational manifold are included in the basis set. For instance, the basis set described above can be represented using this notation as $\{8, 4\}$. Each of these levels possess a $2j + 1$ degeneracy of states, which means that these eight rovibrational levels correlate to a 60 state basis set. Figures 3.7A,B and C illustrate a sequence of calculations at $E = 5000$ cm^{-1} for the three systems of interest using increasingly larger basis sets. While the $\{8, 4\}$ basis set described above does not appear in these figures, results for the substantially larger basis set $\{14, 8\}$ are shown. The values of five vibrationally inelastic cross sections calculated using the $\{14, 8\}$ basis set show large deviations (up to 25%) relative to other calculations of the same cross sections using larger basis sets. It is quite clear that the "rule of thumb" method for selecting the elements of a $v = 0$ rotationally inelastic scattering basis set can not be transplanted into a vibrationally inelastic problem.

The iterative method used to generate figure 3.7 has produced information which can be used to selected an adequately converged basis set. In each vibrational manifold, new j rotational levels are added to the basis set until scattering calculations become insensitive to the addition of another rotational level from this vibrational manifold. At this point the j=0 rotational level from the next highest vibrational manifold is added to the basis set, and the process is repeated. All of these figures illustrate a region where inelastic cross sections $(1, 0) - (0, j)$ level out and become insensitive to the addition of further basis elements. The onset of this region typically occurs when the basis set is $\{14, 8, 8\}$. This basis set represents 210 basis states, corresponding to a much larger problem than the 60 basis states of the $\{8, 4\}$ basis set. Figure 3.9 illustrates the scat-

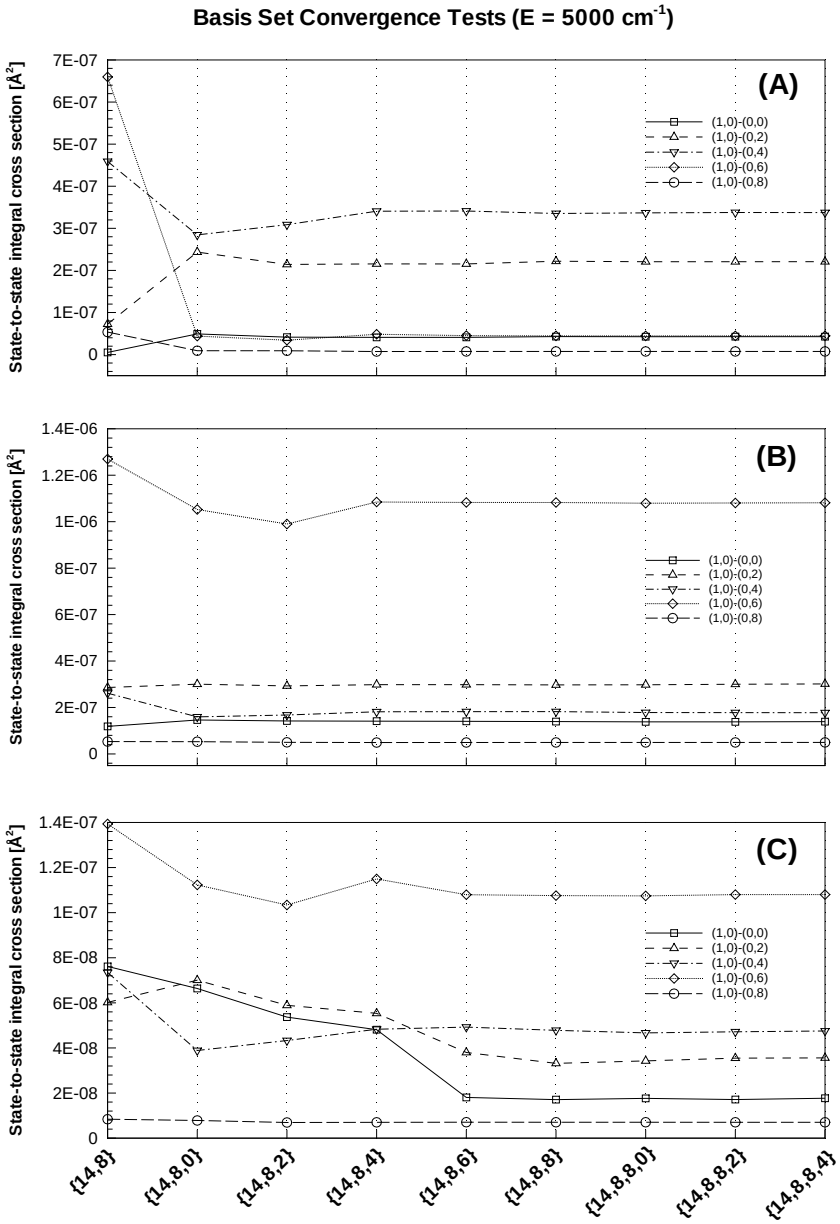

Figure 3.7: The basis set convergence tests at $E = 5000$ cm^{-1} for; **(A)** H_2-He, **(B)** H_2-Ne and **(C)** H_2-Ar.

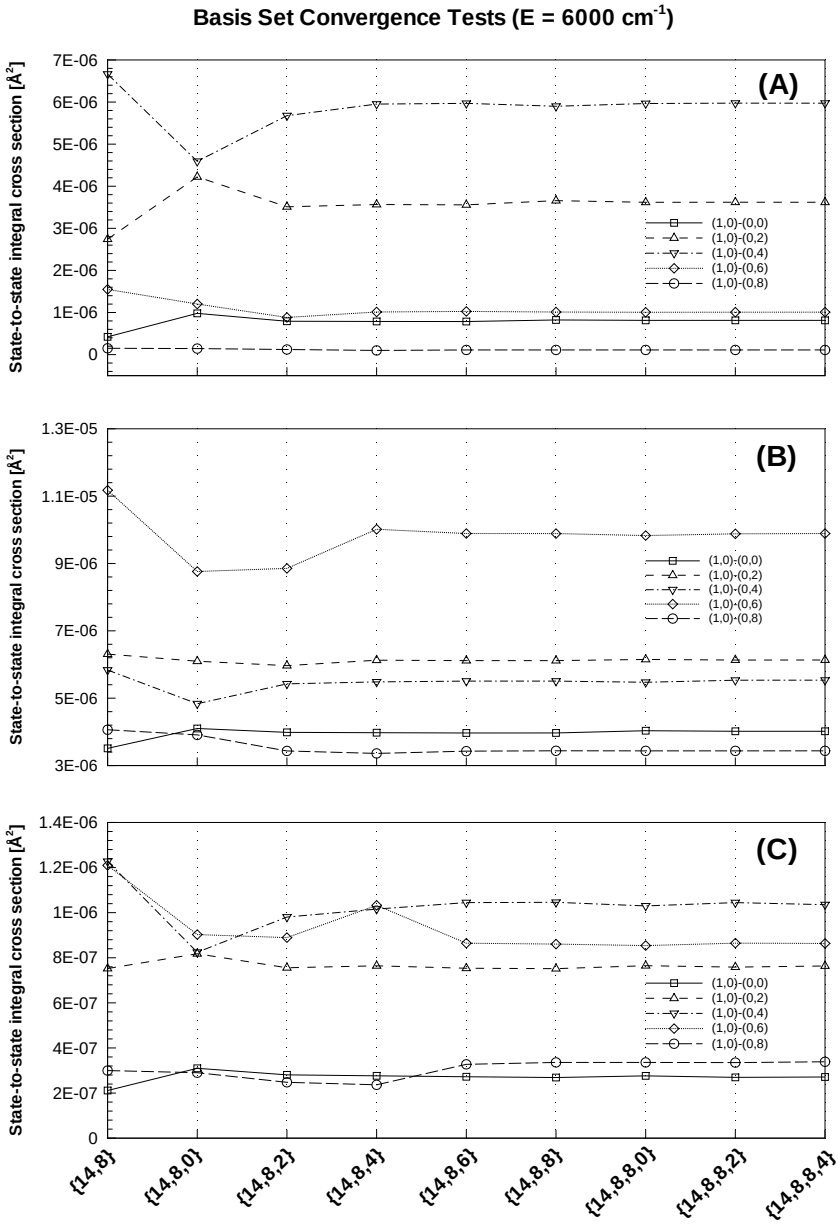

Figure 3.8: The basis set convergence tests at $E = 6000$ cm^{-1} for; **(A)** H_2-He, **(B)** H_2-Ne and **(C)** H_2-Ar.

tering calculation duration in minutes as a function of the basis set size. Notice that the duration of the scattering calculations depends on the basis set size as well as the noble gas collision partner.

Another basis set convergence test at $E = 6000$ cm^{-1} was conducted to determine if there was a basis set dependence on the scattering energy. Figure 3.8 illustrates the same convergence behaviour starting at $\{14, 8, 8\}$ as that found in figure 3.7, showing that the basis set does not significantly depend upon modest changes in the scattering energy. In general, the basis set size *is* dependent upon the scattering energy, the higher the scattering energy, the more energetically accessible states there will be, and hence additional higher energy basis states will be required. However, for the purposes of this research, `MOLSCAT` calculations are limited to scattering energies between 4161.147 and 7000 cm^{-1} due to time constraints. In this energy range the optimum basis set for the scattering calculations has been chosen to be $\{14, 8, 8\}$, since it generates adequately converged vibrationally inelastic cross sections relatively quickly. Should higher energy cross sections be required, their smooth energy dependence, as demonstrated for E $>$ 6000 cm^{-1} in figure 3.12, lend themselves well to extrapolation using Padé approximants [42].

3.4.2 Integration Parameters

One of the attractive features of `MOLSCAT` is the variety of methods which can be used to solve the close-coupling equations. Version 14 of `MOLSCAT` includes eight different solution methods, referred to as *propagators*. Hutson and Green recommend the Alexander-Manolopoulos modified log-derivative/Airy propagator [43] as a reliable general purpose propagator adequate for most scattering cross section calculations [12]. This propagator is discussed in detail by Alexander and Manolopoulos and, for the sake of brevity, will not be explained here.

Most `MOLSCAT` propagators share three parameters which must be carefully optimised before attempting any calculations; `RMIN`, `RMID` and `RMAX`. The `RMIN` and `RMAX` parameters control, respectively, the near and far atom-diatom separation limits for wavefunction propagations. As mentioned in §2.1, the ultimate goal for any molecular scattering calculation is to determine the

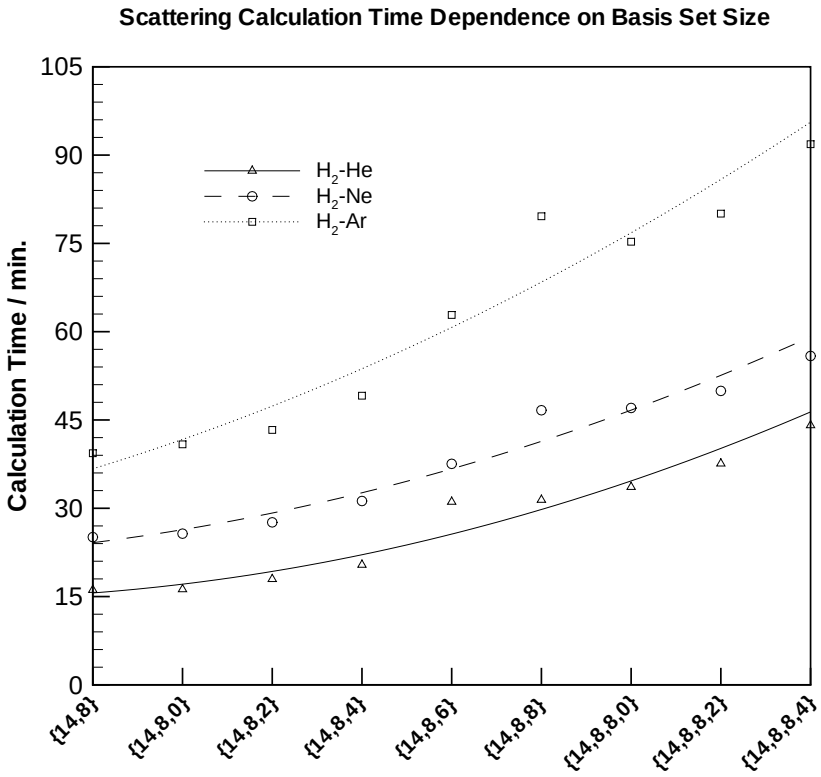

Figure 3.9: The scattering calculation time for the three systems of interest as a function of basis set size (The lines are cubic polynomial fits to demonstrate the general trends).

S-matrix. This is achieved by carefully comparing the asymptotic forms of the wavefunctions evaluated in the presence of the scattering potential to those evaluated in its absence. Clearly if `RMAX` is not set large enough, the wavefunctions will not be propagated to large enough atom-diatom separations to yield a reliable description of the asymptotic part of the wavefunction. The default value of `RMAX` is 10 Å, which is used automatically if `RMAX` is not defined by the user. As demonstrated by the convergence tests at $E = 5000$ and 6000 cm^{-1} (shown in figures 3.10 and 3.11 respectively), this default value represents a nicely converged value for all system of interest, except H_2-Ar at $E = 5000$ cm^{-1}. For the sake of uniformity, `RMAX` has been set to 16 Å for all three systems.

The value of `RMIN` is more of a user-defined guess, and as such, the calculations are much less sensitive to its value. During a calculation, `MOLSCAT` uses the value of `RMIN` provided by the user as a first guess in order to find the inner-turning point of the potential. Once found, it recalculates the wavefunction iteratively at decreasing values of the atom-diatom separation until it finds a converged value of the wavefunction to serve as a starting point for propagation into the classically-allowed region. Because the value `RMIN` isn't directly involved in the calculations, it is not surprising that the resulting cross sections are relatively insensitive to it. Inappropriate values of `RMIN` which are too far away from the inner turning point of the potential will cause an abnormal termination of `MOLSCAT`. Values of `RMIN` = 0.9–1.2 Å have been found to be adequate for the three systems of interest.

The parameter `RMID` is the most nebulous of the three. It represents the atom-diatom separation at which two halves of the propagated wavefunction are matched. Because it is numerically more stable to propagate a wavefunction from a classically-forbidden region into a classically-allowed region than the reverse [12], the inner and outer parts of the wavefunction are respectively propagated from the converged value found near `RMIN` to `RMID`, and from `RMAX` to `RMID`. Any discrepancies between the values and derivatives of the two halves of the wavefunction at `RMID` are used to refine the two halves so that when re-evaluated the two halves match exactly. The

exact location of `RMID` is never clearly defined anywhere in the `MOLSCAT` documentation. The best description found in the documentation states that `RMID` should be located "somewhat beyond the potential minimum" [12]. As long as the value `RMID` is chosen to be at, or slightly beyond, the minimum of the potential well (i.e. `RMID` = 3–4 Å), the calculated cross sections are found not to be significantly sensitive to its exact value.

A set of test scattering calculations of the H_2-He system using the Alexander-Manolopoulos hybrid log-derivative/Airy propagator demonstrates some unpredictable behaviour at low scattering energies (E $<$ 5000 cm^{-1}). Figure 3.12 shows five vibrationally inelastic state-to-state cross sections calculated using two different propagators: the hybrid log-derivative/Airy (HLDA) propagator of Alexander and Manolopoulos [43], and the less sophisticated diabatic modified log-derivative (DMLD) propagator of Manolopoulos [44]. At higher scattering energies the two methods produce results which are nearly indistinguishable. However, as the scattering energy drops below 5000 cm^{-1} the methods begin to produce conflicting results. In particular, the (1,0)-(0,0) and (1,0)-(0,2) state-to-state total integral cross sections calculated using the two methods exhibit distinctly different behaviours in this low energy region. In this region, these cross sections demonstrate a broad resonance-like oscillatory behaviour when calculated using the hybrid log-derivative/Airy propagator, or a smooth near-exponential increase when calculated using the diabatic modified log-derivative propagator (Figure 3.12). To reconcile this difference, vibrationally inelastic scattering calculations of Balakrishnan *et al.* [45], which use the R-matrix propagator of Stechel *et al.* [46], has been investigated. The Balakrishnan *et al.* calculations do not exhibit the same oscillatory low energy cross section behaviour that is present in the cross sections calculated using the hybrid log-derivative/Airy propagator. The best qualitative agreement with the Balakrishnan *et al.* data is found to be the cross section calculated using the DMLD propagator. It is unclear what is responsible for these low energy oscillations seen in the (1,0)-(0,0) and (1,0)-(0,2) cross sections calculated using the HLDA propagator. However, because these oscillations are not found in any of the other calculations, it is believed that they are artifactual and demonstrate a shortcoming of the HLDA propagator in the context of these vibrationally inelastic calculations.

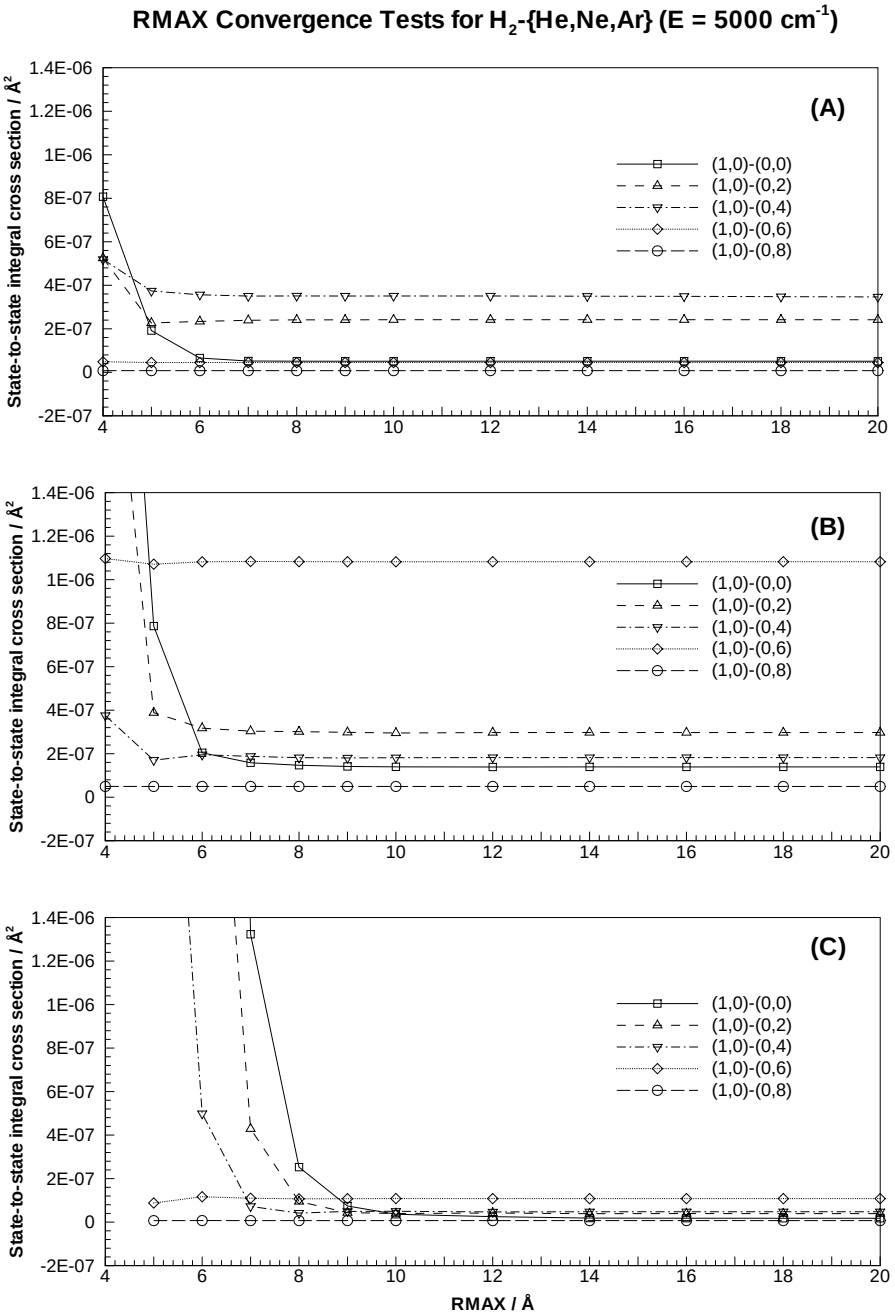

Figure 3.10: RMAX convergence tests at E = 5000 cm^{-1} for; **(A)** H_2-He, **(B)** H_2-Ne, and **(C)** H_2-Ar.

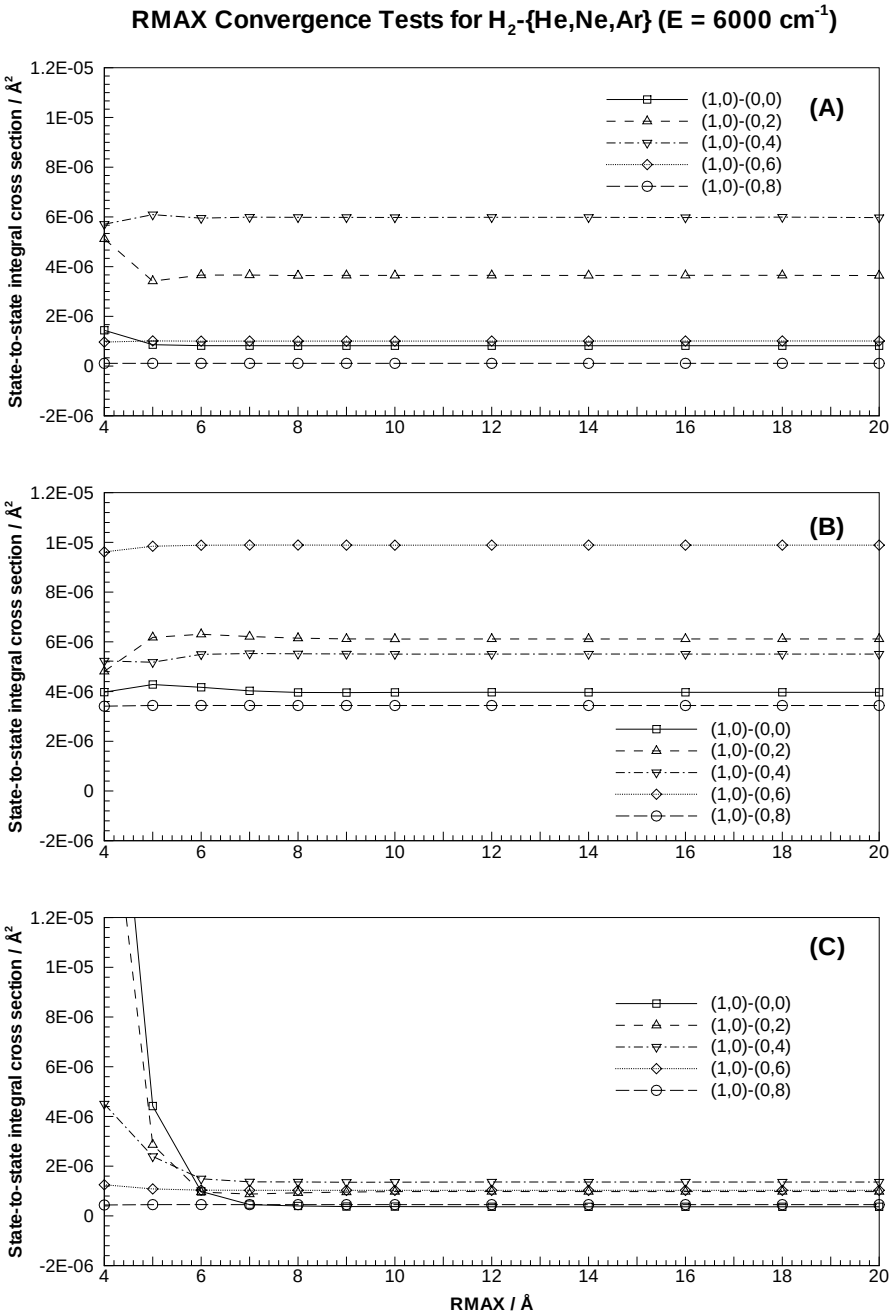

Figure 3.11: RMAX convergence tests at E = 6000 cm^{-1} for; **(A)** H_2-He, **(B)** H_2-Ne, and **(C)** H_2-Ar.

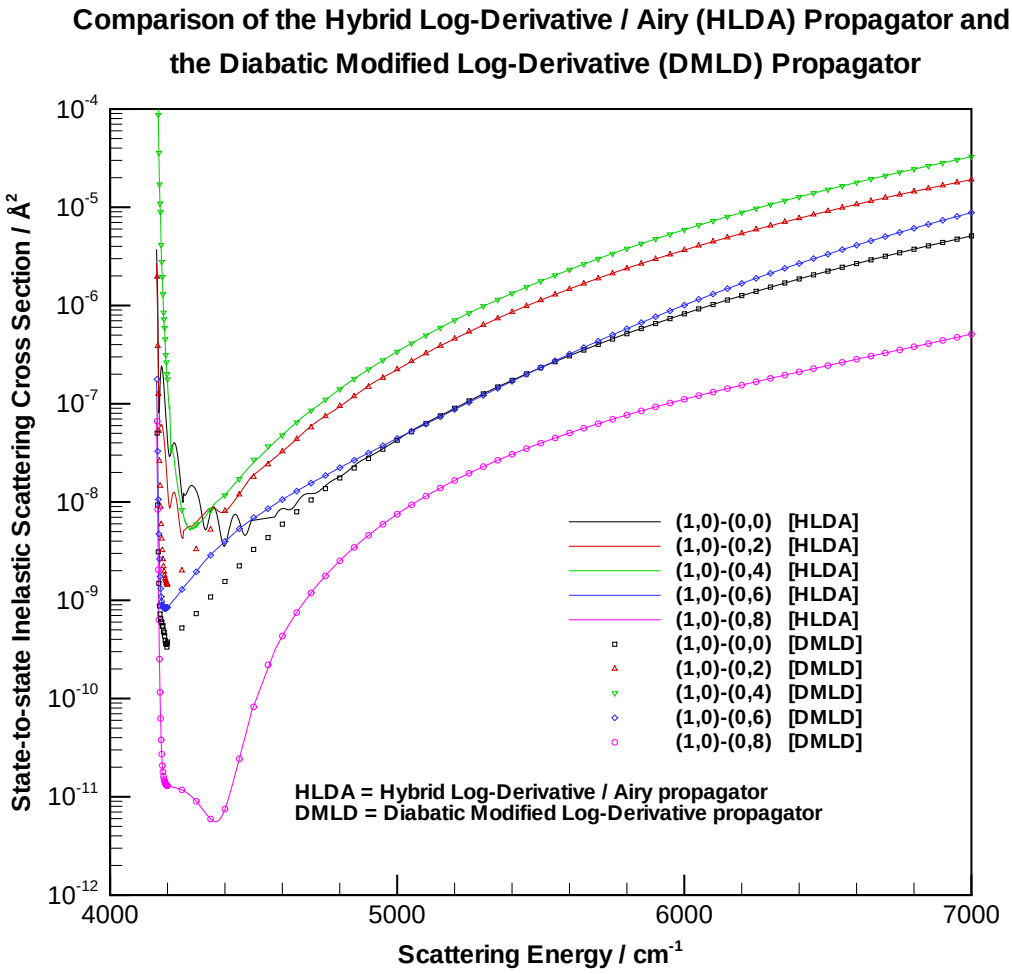

Figure 3.12: Test calculations of H_2-He using two different propagators; the hybrid log-derivative/Airy (HLDA) propagator of Alexander and Manolopoulos [43] (lines), and the diabatic modified log-derivative (DMLD) propagator of Manolopoulos [44] (symbols). Note the discrepancy between the two calculations in the (1,0)-(0,0) and (1,0)-(0,2) cross sections at E $<$ 5000 cm^{-1}.

For this reason, the hybrid log-derivative/Airy propagator has been abandoned in favour of the more reliable diabatic modified log-derivative propagator.

As an example of the calculations using this propagator, figure 3.13 illustrates the energy dependence of the manifold of state-to-state total integral cross sections used in the H_2-Ne calculations. Notice that there is one additional cross section originating from the initial state $v = 1, j = 6$. This is due to the fact that the $v = 0, j = 10$ rovibrational state only satisfies the vibrational relaxation criteria for initial rovibrational levels greater than (or equal to) $v = 1, j = 6$. Final state $v' = 0, j' = 8$ and $v' = 0, j' = 10$ rovibrational levels have also been included on this figure to provide the reader with a better understanding as to the energetically- and rotationally-closest final rovibrational states.

3.5 Thermal Averaging and Rate Constants

The calculated state-to-state total integral cross sections must now be thermally averaged and converted into rate constants. Theoretically, the expression for the thermally averaged state-to-state rate constant involves the energy integration of the product of the state-to-state total integral cross sections and an energy-dependent population factor. Strictly speaking, integration requires that the integrand be a continous function over this range. While the energy-dependent population factor is a continuous function over the range of integration, the discrete representation of the state-to-state total integral cross sections are not. These cross sections are generated by individual `MOLSCAT` calculations performed at a particular scattering energy. This discrete representation of the energy dependence of the cross sections indicates that a straight-forward analytic integration can not be employed to evalute these integrals. In its place a numerical integration method must be used. There are dozens of different methods of performing numerical integration which range in complexity and accuracy [42, 47]. One of the simplest methods is called trapezoidal integration, where the value of the integrand between two discrete values is approximated by a linear line segment. By connecting all of the discrete values of the integrand by such line seg-

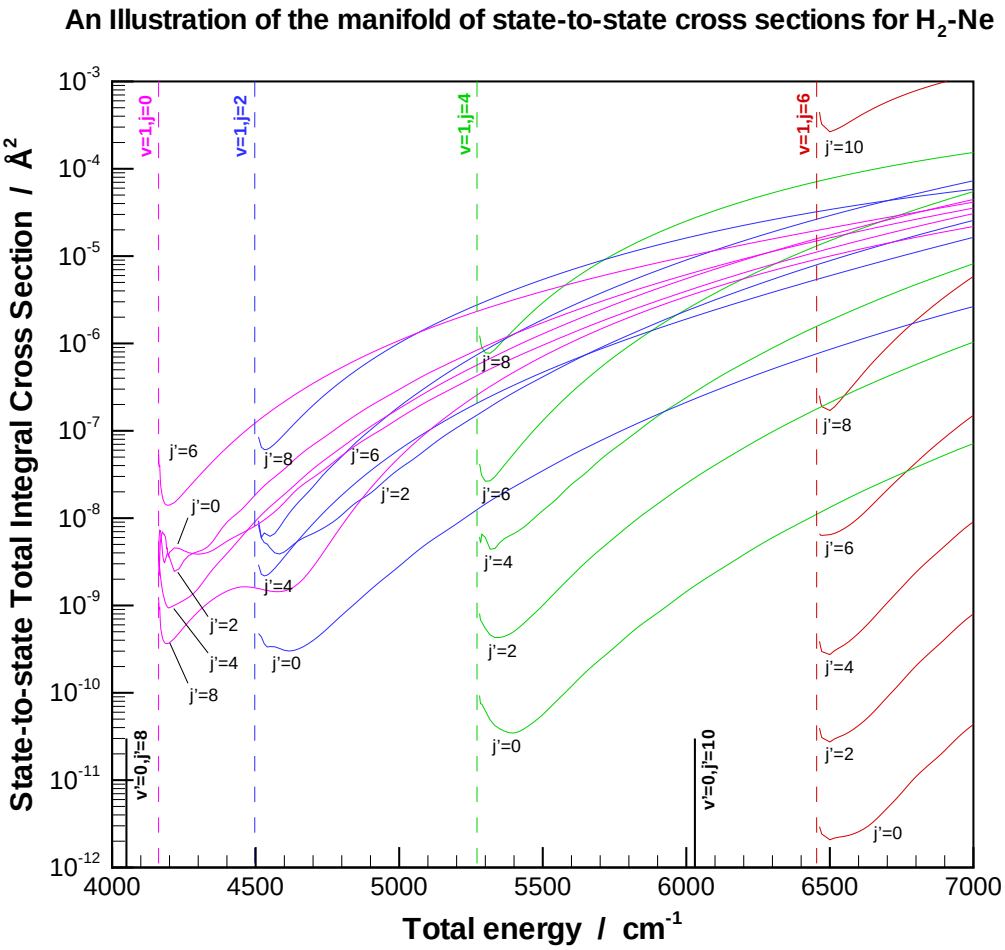

Figure 3.13: An illustration of the manifold of state-to-state total integral cross sections used to construct the manifold-to-manifol vibrational relaxation rate constant for H_2-Ne. Notice the extra cross section originating in the $v = 1, j = 6$ initial rovibrational state.

ments, a piece-wise analytical integration of the integrand can be performed. The spacing of these discrete values is very important. The more discrete points used in the integration routine, the more accurate the ultimate value of the integral will be. However, since each discrete point of the integrand requires one complete `MOLSCAT` calculation, and these calculations can take anywhere between 15 and 90 minutes to complete, this added numerical accuracy requires a considerable investment in cpu time.

Equations 2.19 and 2.17 both involve integration over the energy interval $[0,\infty)$. Clearly, the infinite upper limit is going to pose a problem for the iterative trapezoidal integration method. The integrand in these expressions contains a thermal population factor which has some useful properties. At low temperatures this population factor reaches its maximum value at relatively low energies and decays to zero fairly quickly, while at higher temperatures the maximum occurs at higher energies and decays to zero much slower. Figure 3.14 illustrates the integrand at three different temperatures, $T = 100, 200$ and 250 K. Notice that at $E = 7000$ cm^{-1} the integrand corresponding to $T = 250$ K is adequately converged and the lower temperature integrands are also highly converged. By ensuring that the integrand corresponding to the highest temperature is adequately converged, the convergence of all lower temperature integrands is assured. The highest temperature required herein is 1500 K, requiring an upper integration limit of $\sim 25,000$ cm^{-1} for convergence. The rate constants for all temperatures have been evaluated with this new upper limit. Directing attention now to the lower integration limit, it can be seen in figure 3.14 that the integrand is equal to zero until the scattering energy reaches the energy threshold of the $v = 1, j = 0$ H_2 rovibrational level. Since the integrand below this energy is zero, it will not contribute anything to the value of the rate constant and the lower integration limit can be safely set from 0 to 4161.147 cm^{-1}.

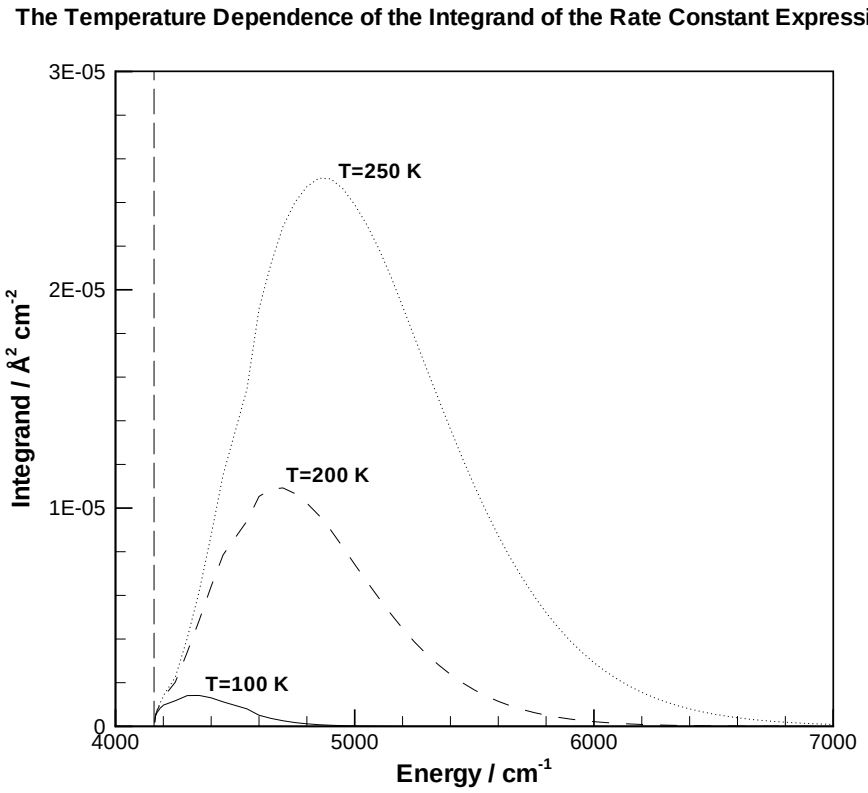

Figure 3.14: The energy dependence of the integrand of the rate constant expressions (2.19 and 2.17) at three different temperatures. Note that at E=7000 cm^{-1}, where the 250 K integrand is converged, both of the other lower temperature integrands are already well converged. The vertical dashed line represents the $v = 1, j = 0$ energy threshold, below which the integrands are zero.

Chapter 4

Results and Discussion

Before proceeding into a thorough discussion of the present results, a brief account of previous research efforts in this field is in order. Research in the field of H_2-Ng vibrational relaxation was quite active in the mid- to late seventies; at that time modern scientific computing was still in its infancy and the processing power available was inadequate for the tasks at hand. The advent of various approximation schemes such as the coupled states [48], infinite order sudden [49] and effective potential [50] methods offered researchers a mechanism to reduce the needed computer power by sacrificing a certain amount of accuracy. Judging by the general lack of publications, H_2-Ng vibrational relaxation seemed to be an unfashionable topic for most of the eighties and the early nineties. Only recently, with the unprecedented leaps in technology, has the processing power been available to solve the un-approximated close coupling equations in a reasonable amount of time. Now as the theorists' interest in this field grows, one would hope that it would only be a matter of time before experimentalists follow suit.

For the sake of brevity, graphical representations of the previous experimental and theoretical data will be suppressed until the current results are ready to be discussed (§4.3). This will consolidate all of the various pieces of data onto one plot for each system.

4.1 Previous Experimental Results

In the mid 1970's Dove and Teitelbaum carried out an extensive set of H_2-{He,Ne,Ar,Kr,Xe and H_2} vibrational relaxation measurements using a high temperature shock-tube apparatus [51]. The shock tube method employs a supersonic shockwave to thermally populate vibrationally excited states of the H_2 diatom. As the shockwave passes, the translational and rotational excitations quickly relax back to their thermal equilibrium distributions leaving only the vibrational motion of the diatom in a state out of thermal-equilibrium. This vibrational motion corresponds to a small but measurable decrease in the index of refraction of the sample gas. When the vibrationally excited diatoms relax back to their thermal equilibrium distribution, the rate of this relaxation process can be monitored by studying the corresponding changes to the index of refraction of the sample gas. The shock-tube method has a few drawbacks which should be mentioned. Shock-tube methods can only produce high temperature shock waves; this is problematic because, as described earlier in SS2.2, high temperature systems require relatively high energy scattering calculations to ensure that the integrand in the rate constant expression is adequately converged. This means that high temperature experimental data is very cpu-intensive to model. In addition, some of these high temperature shock waves have sufficient thermal energy to excite H_2 diatoms into multiply-excited, $v > 1$, vibrational levels, which for other theoretical treatments is not a problem, but lies beyond the current theoretical treatment.

In their work, Dove and Teitelbaum only carried out measurements for a 75% *ortho*-H_2 and 25% *para*-H_2 mixture which is referred to as *normal*-H_2. Only the *para* spin modification of H_2 has been investigated in this work, which means that any comparison between theory and experiment must take into consideration the effect of these different spin modifications. At higher temperatures (> 300 K), the relative contributions of the *ortho* and *para* spin modifications of H_2 to the overall relaxation rate are equivalent [52], thereby making the overall relaxation time identical to that of either *ortho*-H_2 or *para*-H_2. This means that the high temperature *normal*-H_2-Ng relaxation times measured by Dove and Teitelbaum will serve as a good comparison for the calculated *para*-H_2-Ng data presented here. At temperatures lower than 300 K, the relaxation

times for *ortho*- and *para*-H_2-Ng are different, and the low temperature extrapolations of Dove and Teitelbaum will not be useful. Not all of the systems that Dove and Teitelbaum measured are relevant to the current work.

Below are the results of their measurements for *normal*-H_2-He, *normal*-H_2-Ne and *normal*-H_2-Ar represented in terms of the standard relaxation time, $p\tau$ (with units of atm·s), as a function of temperature T (in K),

$$p\tau_{H_2-He} = \exp\left[(41.35 \pm 0.80)T^{-1/3} - (8.984 \pm 0.063)\right], \quad (4.1)$$

$$p\tau_{H_2-Ne} = \exp\left[(28.43 \pm 0.47)T^{-1/3} - (8.094 \pm 0.036)\right], \quad (4.2)$$

$$p\tau_{H_2-Ar} = \exp\left[(45.09 \pm 0.56)T^{-1/3} - (8.956 \pm 0.044)\right]. \quad (4.3)$$

Back in the 1970's, the standard relaxation time was the preferred quantity used by physicists to describe relaxation phenomenon but now, with the increased influence of chemical kinetics, the standard relaxation time has largely been superseded by the notion of rate constants measured in cm^3s^{-1}. A method of converting results quoted in terms of standard relaxation times (in atm·s) to rate constants (in cm^3s^{-1}) begins with the relation,

$$k = \frac{1}{n\tau}, \quad (4.4)$$

where k is the rate constant in cm^3s^{-1}, n is the H_2 number density in cm^{-3} and τ is the relaxation time in s. To determine the value of the number density, consider the isochoric ideal gas relation,

$$\frac{P}{P_0} = \frac{nT}{n_0T_0}, \quad (4.5)$$

where P, n and T are pressure (in atm), number density (in cm^{-3}) and temperature (in K) respectively, and the remaining parameters P_0, n_0 and T_0 represent the standard pressure of 1 atm, Loschmidt's number 2.6867775×10^{19} cm^{-3} and the standard temperature 273.15 K, respectively.

Rearranging for n, gives

$$n = \frac{n_0 T_0 p}{T}, \tag{4.6}$$

where $p = P/P_0$. Substituting back into equation 4.4,

$$k = \frac{T}{n_0 T_0 p \tau} = \frac{T}{7.3389327 \times 10^{21} p \tau}. \tag{4.7}$$

This relation will be used henceforth to convert all experimental data documented in terms of the standard relaxation time into rate constants.

A moderately low temperature study of *normal*-H_2-{He,Ar} by Audibert *et al.* [53] using Raman excitation methods reports values of the standard relaxation times for both systems at 300 K. Their measurements were performed by directing a ruby laser beam into a cell filled with H_2 gas. Raman scattering of the laser beam from the H_2 gas in this cell produces an intense Stokes beam which is then redirected into the sample cell containing the H_2-{He,Ar} gas mixture where it induces vibrational excitations of the H_2 molecules therein. A second laser is passed through this sample cell to measure the index of refraction changes as the vibrationally excited H_2 molecules relax back to their ground vibrational states. Audibert *et al.* do not isolate the two independent spin modifications of H_2 in their experiments, and hence the data represent the combined relaxation of both *para*-H_2 and *ortho*-H_2. At 300K, the effect of these two independent spin modifications of H_2 is difficult to determine, since at this temperature the vibrational relaxation rate constants for the two spin modifications begin to diverge, according to Flower *et al.* [52]. Nonetheless, these data may still be significant to the present work, and hence will be included in the analysis. The standard relaxation times for H_2-He and H_2-Ar are reported as 2.280×10^{-3} atm·s and 7.150×10^{-3} atm·s respectively. In 1976, Audibert *et al.* conducted another similar set of low temperature vibrational relaxation measurements in which they isolated the two spin modifications of H_2 and conducted individual measurements of both *ortho*- and *para*-H_2-He for temperatures between 50 and 300 K [54]. The *ortho*-H_2-He results are not relevant to the current discussion and will not be discussed here. The *para*-H_2-He measurements are hoped to be of suf-

ficient quality to provide a reliable indicator of the low temperature behaviour of the vibrational relaxation rate constant, since the reliability of the extrapolated Dove-Teitelbaum data at such low temperatures is unknown.

Unfortunately there has been very little experimental interest in studying the vibrational relaxation of H_2-Ne. The measurements of Dove and Teitelbaum [51] seem to be the only source of experimental measurements available for this system.

4.2 Previous Theoretical Results

Comparison between theoretical and experimental data is a truism of nearly all scientific disciplines and this field is no exception. Hence, it should not be surprising that the level of interest in these H_2-Ng system exhibited by the experimental community is mirrored to a certain extent by the theoretical community.

In 1981, Orlikowski carried out close-coupling vibrational relaxation calculations [9] for *para*-H_2-He using a variant of the Tsapline-Kutzelnigg potential energy surface [55] which had been modified using data from Raczkowski and Lester [56]. His scattering calculations ranged in total energy from 0.54 eV ($\approx$ 4355 cm^{-1}) to 1.5 eV ($\approx$ 12,100 cm^{-1}), and employed the numerical techniques of Gordon [37, 57]. These calculations incorporated two different basis sets; one for $0.54 < E < 0.9$ eV consisting of {6,5[sic],0}, and another for total energies of $0.9 < E < 1.5$ eV consisting of {8,6,4,0}. One must assume that v=1 j=5 rotational level in the low energy basis set is a typo, as such it assumed to be v=1, j=6 instead. Six manifold-to-manifold vibrational relaxation rate constants were calculated at temperatures 50, 83, 111, 152, 208 and 296 K using the same thermal averaging treatment that is found in §2.2. His calculations seem to compare well with the experimental data of Audibert *et al.* [58] and Dove and Teitelbaum [51], despite the unusual energy and temperature ranges used in his calculations. The low temperature calculations are suspicious because of the rather large value of the total energy at which he has chosen to

begin his calculations. The lowest total energy he used is $E \approx 4355$ cm^{-1}, which corresponds to a kinetic energy of $E_k \approx 200$ cm^{-1}. Several ultra-low kinetic energy scattering calculation studies by Balakrishnan *et al.* [45, 59, 60] and Forrey *et al.* [61] indicate a significant increase in the magnitude of the state-to-state total integral cross sections in this low kinetic energy region that has been omitted by Orlikowski. By omitting the low kinetic energy region from his scattering calculations, Orlikowski has lost all of the information that these low kinetic energy cross sections would have supplied to the rate constant expression. The behaviour of these cross sections at low kinetic energies is very important when it comes to calculating low temperature vibrational relaxation rate constants, because at these low temperatures, only the low energy regions of the state-to-state total integral cross sections are significantly weighted. As a result, Orlikowski's low temperature rate constants should be treated with caution.

Another calculation of the manifold-to-manifold vibrational relaxation rate constant of *para*-H_2-He has been carried out by Flower *et al.* [52]. Like Orlikowski, they conducted close-coupling scattering calculations. However, instead of using the modified Tsapline-Kutzelnigg potential energy surface they chose to employ the *ab initio* Muchnick-Russek potential energy surface [17] instead. For their calculations they have constructed a large scattering basis set which includes all rovibrational levels of *para*-H_2 with energies less than 20,000 K ($\approx$ 14,000 cm^{-1}). This corresponds to a basis set of {16,12,10,8} in the brace notation, some 355 individual basis states! Using this basis set, their scattering calculations have been distributed unevenly over a range of kinetic temperatures from 100 to 60,000 K. These kinetic temperatures correspond to total energies of approximately 4230 cm^{-1} to 42,000 cm^{-1} respectively. The original publication does not contain the entire dataset needed to reproduce their calculations, but upon request Flower graciously supplied their entire dataset for *para*-H_2-He for use in the present analysis [62]. They have carried out their calculations using the de Vogelaere [63], hybrid log-derivative / Airy [43], and R-matrix [46] propagators using the same energy mesh and basis set for each propagator, and obtained mutually consistent results. Their calculations seem to compare well with both the high temperature experimental work of Dove and Teitelbaum and low temperature experimental work

of Audibert *et al.*. However, as discussed below, the low temperature agreement with Audibert *et al.* is likely a coincidence, since there is a significant portion of the important low energy cross section data missing from their calculations. By starting their calculations at a total energy of 4230 cm^{-1} Flower *et al.* have regrettably made the same mistake that Orlikowski made 17 years earlier. This choice of starting energy is too high to incorporate the near-threshold structure of the state-to-state total integral cross sections; consequently, the low temperature rate constants calculated by Flower *et al.* may be of dubious quality. While Flower *et al.* have incorporated lower energies than Orlikowski did, the bulk of the near-threshold cross section information is still left unaccounted for by starting their calculations at 4230 cm^{-1}. For this reason, their 100 K manifold-to-manifold rate constant is probably unrealistic.

At higher temperatures however, the Flower *et al.* calculated rate constant data is thought to be very reliable because of the large basis set that they have used. This basis set includes many highly rotationally excited H_2 states that are not found in the present work. These additional rotational levels provide more initial rovibrational levels from which the H_2 molecule can vibrationally relax. In order to simplify the discussion, let's introduce the notion of a *relaxation pathway*. A relaxation pathway, in the context of this work, is henceforth defined as any diatomic rovibrational transition which meets the vibrational relaxation criterion which was defined earlier. It will also be useful to define the "energy" of these vibrational relaxation pathways as the energy of the initial rovibrational level associated with a pathway. By including more initial rotational levels in the $v = 1$ manifold, Flower *et al.* have incorporated more vibrational relaxation pathways. In comparison to the current work, Flower *et al.* have included all of the relaxation pathways which the current work does, plus 21 additional relaxation pathways. While these additional relaxation pathways (table 4.1) provide many more vibrational relaxation pathways for the H_2 molecule, they only become meaningful when the initial rovibrational level for the pathway is energetically accessible. For rovibrational levels (1,8), (1,10) and (1,12) the corresponding energies of the initial rovibrational levels for these additional relaxation pathways are 8007.573, 9883.733 and 12,031.608 cm^{-1}, respectively. Despite the fairly large energies seen here, these relaxation

$(v_i, j_i) \rightarrow (v_f, j_f)$	$(v_i, j_i) \rightarrow (v_f, j_f)$	$(v_i, j_i) \rightarrow (v_f, j_f)$
(1,8)→(0,0)	(1,10)→(0,0)	(1,12)→(0,0)
(1,8)→(0,2)	(1,10)→(0,2)	(1,12)→(0,2)
(1,8)→(0,4)	(1,10)→(0,4)	(1,12)→(0,4)
(1,8)→(0,6)	(1,10)→(0,6)	(1,12)→(0,6)
(1,8)→(0,8)	(1,10)→(0,8)	(1,12)→(0,8)
(1,8)→(0,10)†	(1,10)→(0,10)	(1,12)→(0,10)
	(1,10)→(0,12)†	(1,12)→(0,12)
		(1,12)→(0,14)†

Table 4.1: Additional vibrational relaxation pathways included in the calculations by Flower *et al.* [52]

pathways will be shown to be very important to the overall relaxation process.

The transitions in table 4.1 labelled with a dagger (†) represent vibrational relaxation pathways which the Flower *et al.* calculations indicate to be the dominant relaxation pathway from that initial rovibrational level. Their data suggest that relaxation pathways which transfer the smallest amount of kinetic energy to the noble gas collision partner are far more probable than the relaxation pathways which transfer larger amounts of kinetic energy. These dominant pathways are shown to be 20–200,000,000 times more probable than any other pathway originating from the same initial rovibrational level! The consequence of these large probabilities is that, despite the small thermal populations of the initial rovibrational levels associated with these relaxation pathways, their contribution to the overall relaxation process can be significant, even at modest temperatures. This seems to indicate the presence of an additional basis set convergence criterion which has been hitherto unaddressed. Not only must the scattering basis set be selected sufficiently large so that the scattering calculations produce converged cross sections, but the basis set must also incorporate sufficient rovibrational levels so that a converged representation of all accessible vibrational relaxation pathways can be constructed.

The low temperature close-coupling work of Lin [64] on H_2-He does not compare well with the other works mentioned here, and as such has been excluded from the current analysis. Other indirectly related works [65, 66, 67, 68, 69, 70] are worth mentioning but do not warrant detailed

Version	E_{lower}	E_{upper}
full	4162.000	25,000.000
Orlikowski	4355.000	25,000.000
Flower	4231.000	25,000.000
Units	cm^{-1}	cm^{-1}

Table 4.2: Energy integration ranges of the "full", "Orlikowski" and "Flower" version of the current vibration relaxation rate constant data.

discussion, due to the various approximation methods which they incorporate.

An exhaustive search of the literature produced no previous theoretical treatments of the $(v = 1)$ manifold-to-manifold vibrational relaxation of either H_2-Ar or H_2-Ne.

4.3 The Current Results

As mentioned earlier, graphical representations of the data from previous vibrational relaxation studies has been withheld until the current data were ready to be discussed. In order to offer the best comparison between data sets, the reader may find that several slightly different incarnations of the same data set appear on the same figure. This is done in order to provide a more meaningful comparison of similar sized datasets, as opposed to just the simplistitic comparison of the overall results.

The accumulated results for H_2-{He,Ne and Ar} are illustrated in figures 4.1, 4.2, and 4.3 respectively. Notice that in figure 4.1, there are three different versions of the current results, and two different versions of the Flower *et al.* results. With regards to the present results, the different versions represent outcomes of the current calculations when different energy integration ranges are used. All three calculations have used slightly different energy ranges, and by modelling the current data using each of these energy ranges a better comparison between datasets is anticipated. Table 4.2 summarises the energy ranges used for each version. Figure 4.1 clearly

illustrates that when the near-threshold state-to-state total integral cross sections are omitted from the calculation, qualitatively more correct low temperature rate constants are produced. The low temperature up-turn of the rate constant seen in the "full" version of the current data is washed away when the near-threshold cross sections are omitted, as is demonstrated by the other versions of the same data. However, neither Orlikowski nor Flower *et al.* ever comment on why they have chosen to omit the near-threshold cross sections from their calculations, and there are no mathematical or physical arguments that have been found to support this omission either. Although the current calculations are more rigorous than the other two (at least in terms of the low temperature, low energy treatment), the improved comparison between the other two calculated results and the experimental measurements suggests the low temperature up-turn of the rate constant may be artificial.

The "full version" of the Flower *et al.* data represents the unmodified results found in table 3 of [52], while the "Weir version" represents a subset of the Flower *et al.* data treated so that only the vibrational relaxation pathways which have been used in the current work are incorporated. This treatment should provide an indicator of the relative importance of the additional relaxation pathways used by Flower *et al.*. The effect of these addition relaxation pathways is quite dramatic, as indicated by the large discrepancy between these two versions of the Flower *et al.* data at high temperatures. The "full" version of the Flower *et al.* data compares quite well with the extrapolated results of Dove and Teitelbaum at higher temperatures, but as the temperature drops, the extrapolated curve of Dove and Teitelbaum and the Flower *et al.* data points begin to differ, which suggests that extrapolation of the Dove and Teitelbaum data below 300–400 K is dangerous.

The discrepancy illustrated by figure 4.1 between the "Flower" version of the current data and the "Weir" version of the Flower *et al.* data is not so easy to quantify. Despite various manipulations which have been attempted in order to make each dataset emulate the other, there still exist two major irreconcilable differences between them, specifically, the difference of potential energy surfaces and the difference in size of the basis sets.

It is difficult, if not impossible, to say which of these is the dominant effect seen here without further investigation. Some follow-up calculations using the Russek-Muchnick H_2-He potential energy surface with the current {14,8,8} basis set, and/or calculations using the Schaefer-Köhler potential energy surface with the {16,12,10,8} basis set used by Flower *et al.* could provide valuable information regarding the source of the discrepancy between these two calculations. Until such calculations are performed one can only speculate as to the true source of the discrepancy. In the meantime, some insight may be gained by considering a statement made by Alexander during a previous treatment of this system [65]. He noted that, within the context of his approximate solutions of the close-coupling equations, vibrationally inelastic processes appeared to be extremely sensitive to the choice of potential energy surface. This could suggest that the slightly different representations of the diatom stretching dependence of the Muchnick-Russek, and Shaefer-Köhler potential energy surfaces could be responsible for the discrepancies seen here. The only way to confirm such a statement would be to carry out the previously mentioned follow-up calculations.

Due to the general lack of interest in the vibrational relaxation of H_2-Ne there is only so much information that can be extracted from figure 4.2. The experimental work of Dove and Teitelbaum as seen in figure 4.1 agrees well with the "full" version of the Flower *et al.* data thereby lending credibility to both data sets. Since there are no other theoretical or experimental data for H_2-Ne, the *normal*-H_2-Ne experimental data from Dove and Teitelbaum is assumed to share the same level of credibility that their data for the H_2-He system enjoys. In order to improve the agreement with the Dove and Teitelbaum measurements, a follow-up vibrational relaxation calculation of H_2-Ne using the expanded basis set {16,12,10,8} used by Flower *et al.* would be useful. While the Dove and Teitelbaum experimental data are believed to be reliable at moderate and high temperatures, the low temperature results ($T < 500$ K) will suffer from the low temperature spin modification issues mentioned earlier, in addition to extrapolation errors. Another set of experimental measurments akin to the H_2-He measurements by Audibert *et al.* [53, 58] are needed to provide reliable low temperature vibrational relaxation rate constant data

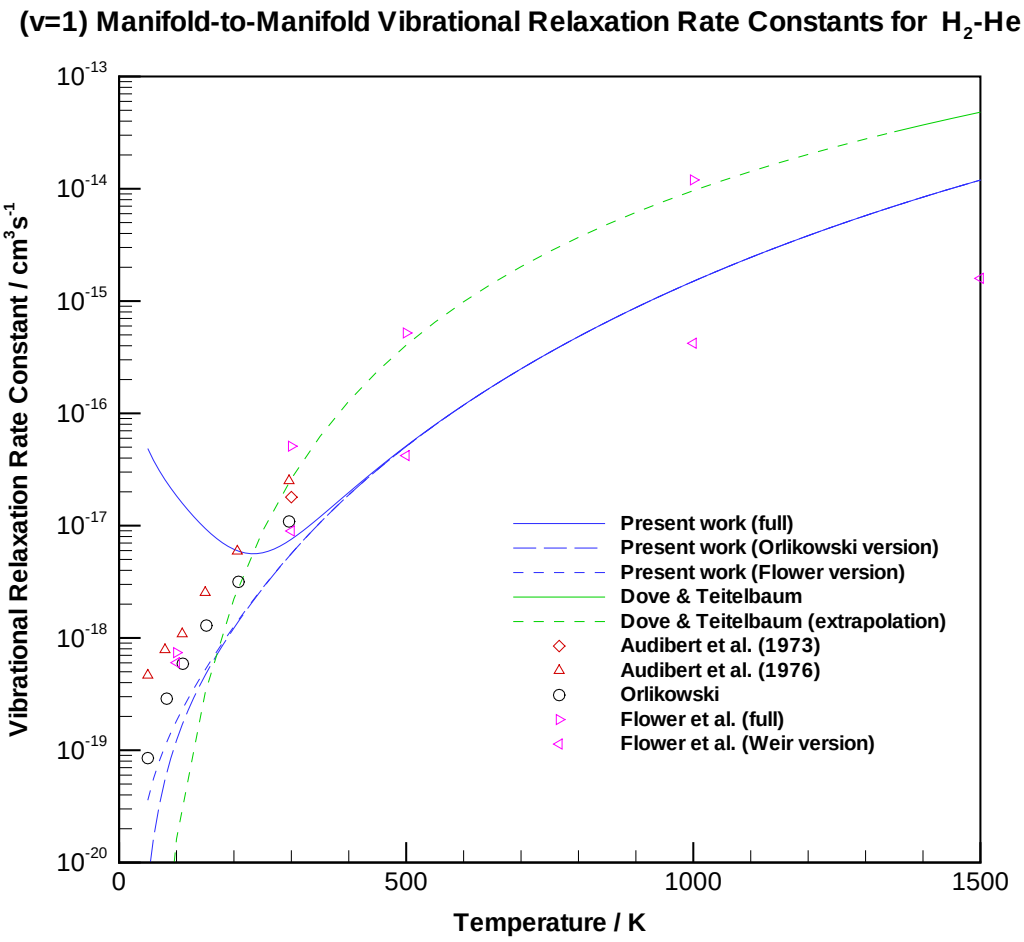

Figure 4.1: ($v = 1$) Manifold-to-manifold vibrational relaxation rate constants for H_2-He.

to complete the experimental description.

The H_2-Ar vibrational relaxation rate constant calculations have not been as successful as they were once hoped they would be. The pathological repulsive wall turn-over found on the H_2-Ar `XC(fit)` potential energy surface was thought to be remedied using a crude *ad hoc* patch. While this was not the best solution, it was the only solution which could be implemented under the given time restrictions. This patched surface enabled successful scattering calculations to be carried out at energies which were previously unattainable. However, despite this patch the scattering calculations still fail, now at a higher energy. During these high energy calculations `MOLSCAT` falters and starts to return very noisy state-to-state total integral cross sections, or fails to report entire cross sections altogether. Generally speaking, at energies beyond 6000 cm^{-1} the state-to-state total integral cross section which it produces are completely unusuable. Of all the cross sections calculated before the scattering calculations failed, only two manifolds of vibrational relaxation cross sections, $(1,0) \rightarrow (0,j)$ and $(1,2) \rightarrow (0,j)$ were salvagable. Because only these two manifolds of relaxation pathways are available, the temperature range of the vibrational relaxation rate constant must be limited to $T < 400$ K (as shown by figure 2.2). At 400 K, this manifold of two initial states can account for 90% of the total initial state population, increasing to 100% as the temperature decreases.

As seen in figure 4.3, the *normal*-H_2-Ar vibrational relaxation rate constant datum of Audibert *et al.* at 300 K agrees well with the extrapolated *normal*-H_2-Ar shock tube measurements of Dove and Teitelbaum. The calculated rate constants from the current work are larger than the experimental results of Dove and Teitelbaum at temperatures below 180 K, but smaller than these results at higher temperatures. At 300 K the rate constants for *ortho*- and *para*-H_2-Ar are likely to begin to differ in the same manner described by Flower *et al.* in their work on *ortho*- and *para*-H_2-He. This means that one should not expect agreement between the *normal*-H_2-Ar experimental measurements and the calculations for *para*-H_2-Ar relaxation times below 300 K. While this spin modification effect can be significant at lower temperatures, it is not believed to

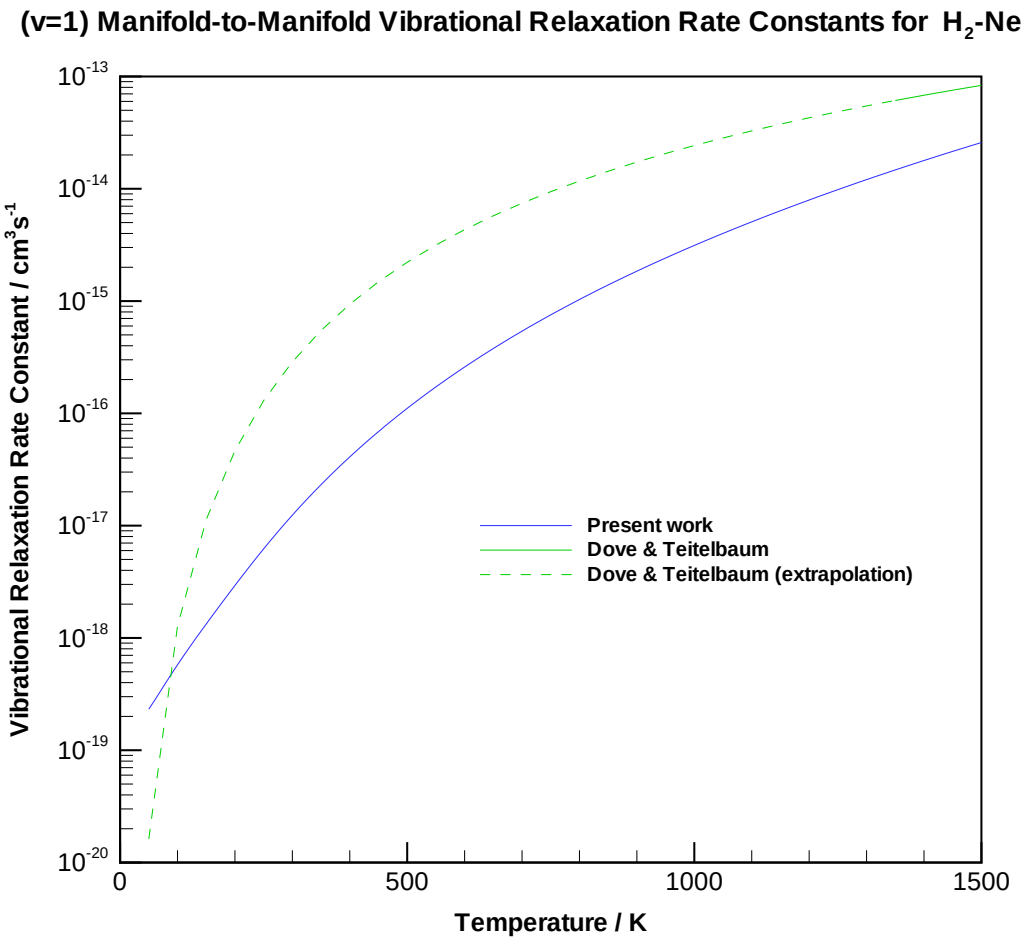

Figure 4.2: ($v = 1$) Manifold-to-manifold vibrational relaxation rate constants for H_2-Ne.

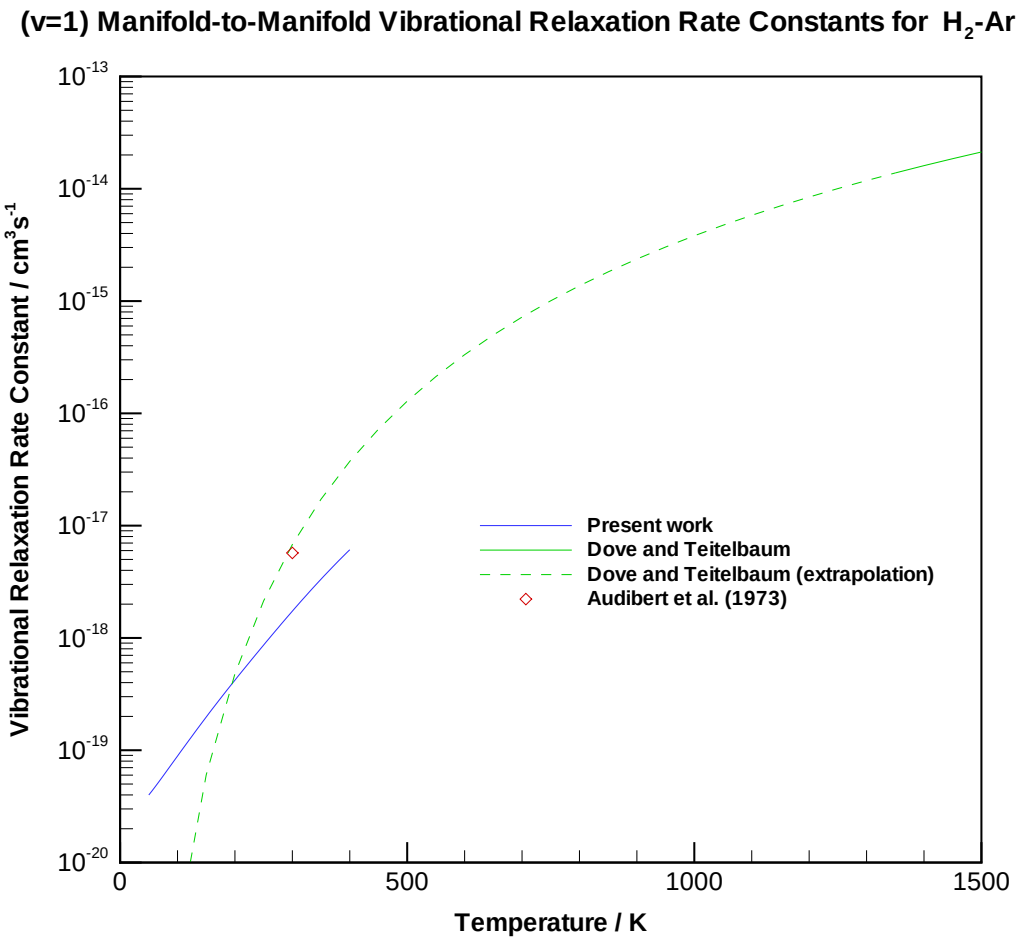

Figure 4.3: ($v = 1$) Manifold-to-manifold vibrational relaxation rate constants for H_2-Ar.

be the major source of the discrepancy seen here, however. By examining figures 4.1, 4.2 and 4.3 some interesting common characteristics emerge. In the high temperature region ($T > 1000$ K) the calculated rate constants for H_2-He and H_2-Ne are approximately one order-of-magnitude below the Dove and Teitelbaum data (as well as the Flower *et al.* data in the case of H_2-He). The H_2-Ar calculations appear to exhibit a similar general trend, which when extended to higher temperatures would lead to a similar order of magnitude discrepancy. Additionally, looking at lower temperatures ($T < 200$ K), the calculated rate constants for H_2-Ne and H_2-Ar cross over the Dove and Teitelbaum data around 100–150 K (as do the "Orlikowski" and "Flower" versions of the H_2-He data). These shared features seem to suggest that the bulk of the discrepancy seen here is caused by a problem which is common to all three systems. The scattering calculations require a different potential energy surface for each system, and it is unlikely that such dissimilar potential energy surfaces could manifest the uniform deviations seen in each of these figures. This may suggest that something else which these systems share in common is the cause of the problems seen here. The two most obvious cultprits are the choice of basis set and manifold of vibrational relaxation pathways.

All three systems share the same basis set and manifold of vibrational relaxation pathways. If one (or both) of these entities were accidentally misconfigured, one would expect to see the effect of this misconfiguration mirrored in the calculations for each system. Unfortunately, there is adequate information to suggest that both the basis set and the manifold of vibrational relaxation pathways used in the current calculations are adequate for the range of energies for which calculations have been made. The basis set convergence tests shown in figures 3.7 and 3.8 indicate that the basis set used here *is* adequately converged, and figure 2.2 demonstrates that most (> 90 %) of the population of vibrationally excited diatoms *is* accounted for by the manifold of vibrational relaxation pathways used in this work. It is possible that there could be yet another source of error, hitherto unaddressed, which is cause of the problems seen here, but first attention should directed toward the basis set and manifold of relaxation pathways shortcomings mentioned here. As mentioned before, further calculations using larger basis sets, higher energies, and larger mani-

folds of relaxation pathways are required to determine the deficiency of the calculations presented here.

In terms of assessing the stretching dependence of the `XC(fit)` H_2-Ar potential energy surface (the motivation which spurred this entire treatise on H_2-Ng vibrational relaxation), it is difficult to say at the present time whether or not the stretching dependence of this surface is inadequate. Further improved calculations featuring larger basis sets and larger manifolds of relaxation pathways are required in order to produce more meaningful data. It would perhaps be unwise to speculate at this point whether or not the work of Bissonnette *et al.* [2] is at fault until the problems associated with the current work are solved.

Chapter 5

Summary

Calculations of the vibrational relaxation manifold-to-manifold rate constant are much more complicated than they were originally thought to be. While similar in principle to rotational relaxation, vibrational relaxation is not just a simple extension which incorporates an additional quantum number. In fact it is a labyrinth of subtle complexity. Concepts like basis-set selection which were steadfastly defined in the context of rotational relaxation, become nebulous and open to interpretation when the discussion shifts to vibrational relaxation. The work presented here represents an informative preliminary attempt at entering the complicated realm of vibrational relaxation, including a beneficial glimpse of some of the pitfalls associated with it.

The calculated vibrational relaxation rate constants for all three systems exhibit a similar discrepancy relative to previous experimental and theoretical works. The relative uniformity of these deviations suggests that a source common to each system is responsible for the problems manifested in figures 4.1, 4.2 and 4.3. The force communicated between scattering partners is described using a potential energy surface. These potential energy surfaces are unique to each system and it is unlikely that they are all deficient in such a way as to produce the relatively uniform discrepancies seen here. However, two potential sources of the problem which are common to all three systems are: (i) the scattering basis set, and (ii) the manifold of relaxation

pathways. Although the {14,8,8} basis set used in this work is believed to be adequate for the energies considered here, the more-extensive basis set used by Flower *et al.* has demonstrated that higher energies and hence large basis sets may well be required. Originally it was believed, based upon thermal population considerations, that these high energy relaxation pathways would be less important than the lower energy pathways. For the temperatures considered in this work, the initial state populations of these high energy relaxation pathways is small but, as the Flower *et al.* data suggest, these relaxation pathways are between 20 and 200,000,000 times stronger than any other relaxation pathway from the same initial state. This means that not only must the scattering basis set be made large enough to provide numerically converged cross sections, but it must also be large enough to include a numerically converged representation of all of the important relaxation pathways.

To improve this work, a set of follow-up calculations are required to further delineate the source of the discrepancy seen in figures 4.1, 4.2 and 4.3. Calculations using larger basis sets such as the {16,12,10,8} used by Flower *et al.* and larger manifolds of relaxation pathways in conjunction with the same potential energy surfaces used here would be immensely helpful. Additional vibrational relaxation calculations of H_2-He featuring the Muchnick-Russek potential energy surface could help highlight the role of the potential energy surface on these calculations - offering quantitative results to the apparent"extreme sensitivity" of such calculations to the potential energy surface [65]. The curtailed results of H_2-Ar are proof positive that a close inspection of the repulsive wall of the `XC(fit)` H_2-Ar potential energy surface is required. Once this potential is repaired the high-energy, larger-basis-set calculations can be performed on this system. Finally, there is a considerable level of underexposure demonstrated by these systems in both the experimental and theoretical communities. The more data collected on these systems, the better our understanding of H_2-Ng vibrational relaxation will be.

Appendix A

H_2-He Parameters

The tables of data presented here represent the complete list of parameters which are needed to reproduce completely the fitted version of the Schaefer-Köhler H_2-He potential energy surface. This fitted potential energy surface is a collection of nine atom-diatom separation functions $W_{\lambda k}(R)$; six of which are represented as modified Lennard-Jones (12,6) potential energy curves, and three of which are represented by repulsive exponential potential energy curves. Table A.1 represents the parameters for the modified Lennard-Jones (12,6) functions while table A.2 represents the parameters for the repulsive exponential functions.

$W_{\lambda k}(R)$		**Parameters**					
λ	k	D_e	R_e	β_0	β_1	β_2	$C_6^{\lambda,k}$
0	0	4.26813(-5)	6.41987	-2.73456(-1)	7.31308	-5.47135	3.06848
0	1	2.00251(-5)	7.15733	4.45680(-1)	9.29232	-7.71810	3.79508
0	2	2.62754(-5)	1.94785	-2.96265	1.89624(+1)	3.56123(+1)	0.00000
2	0	4.64155(-6)	6.85353	1.10391	9.9428	-5.35070	5.67202(-1)
2	1	8.42029(-6)	7.21824	1.83289	1.16304(+1)	-5.47720	1.13977
2	2	7.85607(-6)	7.31394	3.20182	1.92500(+1)	-2.58445	5.20131(-1)
units:		$[E_h]$	$[a_0]$	[0]	[0]	[0]	$[E_h \cdot a_0^6]$

Table A.1: Parameters for the modified Lennard-Jones (12,6) potential components $W_{\lambda k}(R)$. Quantities in parentheses represent powers of 10 in scientific notation representation.

λ	k	$\mathcal{D}_e$	$\mathcal{R}_e$	$\mathcal{B}_0$	$\mathcal{B}_1$	$\mathcal{B}_2$
4	0	5.53125(-4)	3.00000	1.39835(+1)	-4.74600(-1)	1.26365(+1)
4	1	1.57933(-3)	3.00000	1.86265(+1)	2.68669	0.00000
4	2	8.79434(-2)	2.00000	2.04201(+1)	2.28832(+1)	-3.79061(+1)
units:		[E_h]	[a_0]	[0]	[0]	[0]

Table A.2: Parameters for the exponential potential components $W_{4k}(R)$. Quantities in parentheses represent powers of 10 in scientific notation representation.

Bibliography

[1] D. Flower, *Molecular Collisions in the Interstellar Medium* (Cambridge, Cambridge, 1990).

[2] C. Bissonnette, C. E. Chauqui, K. G. Crowell, R. J. LeRoy, R. J. Wheatley, and W. J. Meath, J. Chem. Phys. **105**, 2639 (1996).

[3] L. D. Waldron, *Quantal Calculation of Raman Lineshape Parameters for H_2 and D_2 in Ar*, Master's thesis, University of Waterloo (1998).

[4] J. P. Berger, R. Saint-Loup, H. Berger, J. Bonamy, and D. Robert, Phys. Rev. A **49**, 3396 (1994).

[5] R. S. Berry, S. A. Rice, and J. Ross, *Physical Chemistry, 2nd Ed.* (Oxford, New York, 2000).

[6] A. Arthurs and A. Dalgarno, Proc. R. Soc. London **256**, 540 (1960).

[7] G. Wolken, Jr., W. H. Miller, and M. Karplus, J. Chem. Phys. **56**, 4930 (1972).

[8] W. Lester, Jr., *Dynamics of Molecular Collisions Part A* (Plenum, 1976), pp. 1–32.

[9] T. Orlikowski, Chem. Phys. **61**, 405 (1981).

[10] R. D. Levine and R. B. Bernstein, *Molecular Reaction Dynamics* (Oxford, New York, 1974).

[11] J. C. Maxwell, Phil. Trans. **157**, 49 (1867).

[12] J. M. Hutson and S. Green, `MOLSCAT` computer code v14, Collaborative Computational Project No. 6 of the Engineering and Physical Sciences Research Council (UK) (1994).

[13] HIBRIDON^{TM} is a package of programs for the time-independent quantum treatment of inelastic collisions and photodissociation written by M. H. Alexander, D. E. Manolopoulos, H.-J. Werner, and B. Follmeg, with contributions by P. F. Vohralik, D. Lemoine, G. Corey, R. Gordon, B. Johnson, T. Orlikowski, A. Berning, A. Degli-Esposti, C. Rist, P. Dagdigian, B. Pouilly, G. van der Sanden, M. Yang, and F. de Weerd.

[14] J. Y. Seto, Z. Morbi, F. Charron, S. K. Lee, P. F. Bernath, and R. J. Le Roy, J. Chem. Phys. **110**, 11756 (1999).

[15] J. Y. Seto, R. J. Le Roy, J. Vergès, and C. Amiot, J. Chem. Phys. **113**, 3067 (2000).

[16] J. Schaefer and W. E. Köhler, Physica **129**, 469 (1984).

[17] P. Muchnick and A. Russek, J. Chem. Phys. **100**, 4336 (1994).

[18] K. G. Crowell, *A Reliable New Potential Energy Surface for H_2-Ne*, Master's thesis, University of Waterloo (1996).

[19] W. Meyer, P. C. Hariharan, and W. Kutzelnigg, J. Chem. Phys. **73**, 1880 (1980).

[20] K. C. Ng, W. J. Meath, and A. R. Allnatt, Mol. Phys. **32**, 175 (1978).

[21] K. C. Ng, W. J. Meath, and A. R. Allnatt, Mol. Phys. **37**, 237 (1979).

[22] W. J. Meath, D. J. Margoliash, B. L. Jhanwar, A. Koide, and G. D. Zeiss, in *Intermolecular Forces*, edited by B. Pullman (Reidel, Dordrecht, 1981), 14th Jerusalem Symposium on Quantum Chemistry and Biochemistry, p. 101.

[23] A. K. Dham, F. R. W. McCourt, and W. J. Meath, J. Chem. Phys. **103**, 8477 (1995).

[24] A. K. Dham and W. J. Meath, Chem. Phys. **196**, 125 (1995).

[25] R. J. Le Roy, C. Bissonnette, T. H. Wu, A. K. Dham, and W. J. Meath, Faraday Discuss. Chem. Soc. **97**, 81 (1994).

[26] R. J. Le Roy, J. Mol. Spec. **191**, 223 (1998).

[27] R. J. Le Roy, *Level 7.0 - a computer program solving the radial schrödinger equation for bound and quasibound levels*, University of Waterloo Chemical Physics Report (CP-642) (2000).

[28] C. Schwartz and R. J. Le Roy, J. Mol. Spec. **121**, 420 (1987).

[29] R. J. Le Roy, *A practical guide to least–squares fitting*, University of Waterloo Chemical Physics Report (CP-628) (1997).

[30] A. J. Thakkar, Z.-M. Hu, C. E. Chuaqui, J. S. Carley, and R. J. Le Roy, Theoretica Chimica Acta **82**, 57 (1992).

[31] E. B. Smith, Physica **73**, 211 (1974).

[32] P. G. Hajigeorgiou and R. J. Le Roy, J. Chem. Phys. **112**, 3949 (2000).

[33] P. R. Bevington, *Data Reduction and Error Analysis for the Physical Sciences* (McGraw Hill, New York, 1969).

[34] `http://www.sgi.com/Products/PDF/1150.pdf`.

[35] `http://www.sgi.com/Products/PDF/2500.pdf`.

[36] J. M. Huston, Comp. Phys. Comm. **84**, 1 (1994).

[37] R. G. Gordon, J. Chem. Phys. **51**, 14 (1969).

[38] A. M. Dunker and R. G. Gordon, J. Chem. Phys. **64**, 4984 (1976).

[39] B. R. Johnson, J. Chem. Phys. **67**, 4086 (1977).

[40] M. Shapiro and G. G. Balint-Kurti, J. Chem. Phys. **71**, 1461 (1979).

[41] G. B. Clark, *The Close-Coupled Calculation of Transport Properties for Atom-Diatom Systems*, Master's thesis, University of Waterloo (1999).

[42] R. L. Burden, J. D. Faires, and A. C. Reynolds, *Numerical Analysis, Second Edition* (Prindle, Weber & Schmidt, Massachusetts, 1981).

[43] M. H. Alexander and D. E. Manolopoulos, J. Chem. Phys. **86**, 2044 (1987).

[44] D. E. Manolopoulos, J. Chem. Phys. **85**, 6425 (1986).

[45] N. Balakrishnan, R. C. Forrey, and A. Dalgarno, Phys. Rev. Lett. **80**, 3224 (1998).

[46] E. B. Stechel, R. B. Walker, and J. C. Light, J. Chem. Phys. **69**, 3518 (1978).

[47] W. H. Press, S. A. Teukolsky, W. T. Vetterling, and B. P. Flannery, *Numerical Recipes in C - The Art of Scientific Computing* (Cambridge, Massachusetts, 1997).

[48] P. McGuire and D. J. Kouri, J. Chem. Phys. **60**, 2488 (1974).

[49] R. Goldflam, S. Green, and D. J. Kouri, J. Chem. Phys. **67**, 4149 (1977).

[50] H. Rabitz, J. Chem. Phys. **57**, 1718 (1972).

[51] J. E. Dove and H. Teitelbaum, Chem. Phys. **6**, 431 (1974).

[52] D. R. Flower, E. Roueff, and C. J. Zeippen, J. Phys. B: At. Mol. Opt. Phys. **31**, 1105 (1998).

[53] M.-M. Audibert, C. Joffrin, and J. Ducuing, Chem. Phys. Lett. **19**, 26 (1973).

[54] M.-M. Audibert, J. Lukasik, and J. Ducuing, Chem. Phys. Lett. **37**, 408 (1976).

[55] B. Tsapline and W. Kutzelnigg, Chem. Phys. Lett. **23**, 173 (1973).

[56] A. W. Raczkowski and W. A. Lester, Jr., Chem. Phys. Lett. **47**, 45 (1977).

[57] R. G. Gordon, Meth. Comput. Phys. **10**, 81 (1971).

[58] M.-M. Audibert, C. Joffrin, and J. Ducuing, J. Chem. Phys. **61**, 4357 (1974).

[59] N. Balakrishnan, R. C. Forrey, and A. Dalgarno, Astrophys. J. **514**, 520 (1999).

[60] N. Balakrishnan, M. Viera, J. F. Babb, and A. Dalgarno, Astrophys. J. **524**, 1122 (1999).

[61] R. C. Forrey, V. Kharchenko, N. Balakrishnan, and A. Dalgarno, Phys. Rev. A **59**, 2146 (1999).

[62] D. Flower, *Private communication* (2001).

[63] R. de Vogelaere, J. Res. Nat. Bur. Stand. **54**, 119 (1955).

[64] C. S. Lin, J. Chem. Phys. **73**, 1159 (1980).

[65] M. H. Alexander, Chem. Phys. **8**, 86 (1975).

[66] M. H. Alexander, Chem. Phys. Lett. **38**, 417 (1976).

[67] M. H. Alexander, Chem. Phys. **20**, 83 (1977).

[68] J. E. Dove and S. Raynor, J. Phys. Chem. **83**, 127 (1979).

[69] C. S. Lin and D. Secrest, J. Chem. Phys. **70**, 199 (1979).

[70] C. S. Lin, J. Chem. Phys. **70**, 1791 (1979).